JOURNAL OF SPACECRAFT AND ROCKETS
Vol. 61, No. 1, January–February 2024

Multi-Degree-of-Freedom Active Isolation Platform for Microvibrations

Vicente Lafarga*
Université Libre de Bruxelles, 1050 Brussels, Belgium
Rasa Jamshidi†
Liège University, 4000 Liège, Belgium
Gonçalo Rodrigues‡ and René Seiler§
European Space Agency, 2200 AG Noordwijk, The Netherlands
and
Christophe Collette¶
Université Libre de Bruxelles, 1050 Brussels, Belgium

https://doi.org/10.2514/1.A35550

Reaction wheels are widely used in the attitude control of spacecraft due to their capability of applying control torques, greatly reducing the propellant requirements and limiting its use to reaction wheel desaturation. However, the presence of unavoidable mechanical imperfections results in significant mechanical disturbances, being applied to the spacecraft, which can severely impact the operation of sensitive payloads. These microvibrations are broadband in nature, and therefore the effective mitigation of their effects requires a high isolation factor throughout a wide frequency range. This paper presents the development and experimental verification of a six-degree-of-freedom active isolation platform for a reaction wheel, integrating a soft suspension and active control using self-sensing actuators. A reduction in the transmitted forces of 65 dB at 270 Hz was experimentally demonstrated, while exhibiting negligible amplifications by its suspension resonance, which constitute very attractive performances.

I. Introduction

MECHANICAL disturbances with amplitude of micro- or milli-*g* propagating onboard satellites can be very detrimental to the accomplishment of their missions. These disturbances can compromise the fine pointing required in high-resolution imaging telescopes employed for Earth remote sensing [1], astronomical observations [2], or intersatellite laser communications [3]. But such microvibrations can also increase the noise levels of particular sensitive instruments rendering their measurements useless, as is the case of high-precision accelerometers used in gravimetric missions [4], optical interferometers [5], or reference oscillators [6].

The main sources of microvibrations onboard satellites consist of mechanisms such as cryocoolers, mirror and antenna pointing mechanisms, solar array driving mechanisms, and reaction wheels. In particular, reaction wheels are a prevalent actuator for the attitude control of satellites, which operate by repeatedly transferring angular momentum to and from a flywheel to the spacecraft. To enable attitude change maneuvers with the required agility, the flywheels used have considerable inertia and can operate continuously at high spin rates. Therefore, minor unbalances on their inertia properties and imperfections in the bearings used for flywheel suspension and their internal components originate disturbance forces and moments. These disturbances are broadband, mainly occurring at the spinning rate of the reaction wheels and its harmonics, and propagate through the spacecraft structure being amplified by their lightly damped resonances, finally reaching sensitive instruments with sufficient amplitude to affect their operation. Often, reaction wheels are the largest pointing and vibration disturbance in spacecraft.

Extensive efforts have been carried out for their characterization and modeling, resorting to on-ground tests and flight data by Seiler and Allegranza [7], Liebold et al. [8], and Prashant et al. [9]. A detailed breakdown of the reaction wheel disturbances can be made into its individual components, allowing the synthesis of disturbance models as done by Masterson et al. [10] and Le [11].

The characterization of the disturbance mechanisms is only one part of the management of the microvibration problem. This management needs to take place at system level, including the definition of performance budgets, and the implementation of an engineering process that encompasses simulation, testing, and definition and verification of overall microvibration levels and interface requirements [12–14]. The process for minimizing the microvibration disturbances then involves design and operational aspects. On the design side, sources and receivers should be accommodated within the satellite far away from each other, if allowed by their function. The introduction of damping systems or isolation layers can be considered together with a tradeoff to be performed between sources and receivers. The overlap of frequencies shall be avoided between excitation sources, structural resonant modes, and susceptibilities of receivers. Moreover, this frequency control must be extended to the operational concepts, by scheduling the operation of mechanisms in a way that minimizes the impact of their disturbances. In the case of reaction wheels, this translates into constraining their usable speed range and establishing specific pointing control strategies.

Missions requiring extreme stability resort to microthrusters to actuate their attitude control systems instead of reaction wheels [15]. Such microthrusters produce very limited mechanical disturbances and operate by ejecting cold gas, or by accelerating tiny charged droplets, metallic ions, or plasma by means of an electrical field.

Received 10 September 2022; revision received 20 June 2023; accepted for publication 22 June 2023; published online 25 July 2023.

*Ph.D. Student, Precision Mechatronics Laboratory, Bio-Electro and Mechanical Systems Department, Avenue F.D. Roosevelt 50; vlafarga@ulb.be (Corresponding Author).

†Post-Doctoral Researcher, Precision Mechatronics Laboratory, Department of Aerospace and Mechanical Engineering, Allée de la Découverte 9.

‡Structures Engineer, Structures Section, European Space Research and Technology Centre, Keplerlaan 1.

§Senior Mechanisms Engineer, Mechanisms Section, European Space Research and Technology Centre, Keplerlaan 1.

¶Associate Professor, Precision Mechatronics Laboratory, Bio-Electro and Mechanical Systems Department, Avenue F.D. Roosevelt 50; also Professor, Precision Mechatronics Laboratory, Department of Aerospace and Mechanical Engineering, Allée de la Découverte 9, Université de Liège, 4000 Liège, Belgium.

Dennehy and Alvarez-Salazar [16] have presented an extensive review of challenges, lessons learned, and potential solutions regarding spacecraft microvibrations. The severity of the microvibration problem is ranked in terms of the pointing stability requirements of a mission, and different design solutions are recommended. For instance, reaction wheel isolation platforms are typically necessary for missions with pointing stability in the range between 10 and 0.1 arcsec, which correspond, e.g., to the Chandra X-ray, and the European Space Agency–European Organisation for the Exploitation of Meteorological Satellites Meteosat Third Generation (ESA-EUMETSAT MTG) with its infrared and ultraviolet imagers and sounders. Dual-stage passive isolation is then recommended when pointing stability in the order of 0.01 arcsec is required, e.g., Space Infrared Telescope Facility (SIRTF). And microthrusters become essential for pointing stability better than 0.01 arcsec, such as the case of Global Astrometric Interferometer for Astrophysics (GAIA), the currently under development Nancy Grace Roman Space Telescope, and the more ambitious Habitable Exoplanet Observatory (HABEX) and Large Ultraviolet Optical Infrared Surveyor (LUVOIR).

The drawback of employing microthrusters is that they significantly constrain the design of the spacecraft with a distributed infrastructure, including tubing, reservoirs, and the thrusters themselves. Moreover, the consumable propellant limits the operational lifetime of the spacecraft (SC). Therefore, a strong interest remains to push the envelope of applicability of reaction wheels, and thereby improve the performance of vibration isolation systems capable of filtering the disturbances they create. While passive isolation suspensions have become a recurrent element on space missions requiring high mechanical stability, their enhancement has been sought by introducing sensors and actuators and implementing feed-back control loops.

A. Principle of Vibration Isolation

The principle of a vibration isolation suspension is best illustrated by analyzing the transmissibility of a disturbance from a base structure to a single mass supported by a spring and a dashpot. Transmissibility is defined by the ratio of acceleration between the suspended mass versus that of the base structure. Assuming a linear system and a viscous dashpot, it can be expressed by Eq. (1) and is illustrated on Fig. 1, where X is the resulting motion of the mass to an input base motion X_0, ω is the frequency, ω_n is the natural frequency of the system, and ξ is the damping coefficient of the system that is related to the Q-factor as shown in Eq. (2) [17]. The equivalence between motion and force transmissibility is demonstrated in the Appendix.

$$|X/X_0| = \sqrt{\frac{1}{(1-(\omega^2/\omega_n^2))^2 + (2\xi(\omega/\omega_n))^2}} \tag{1}$$

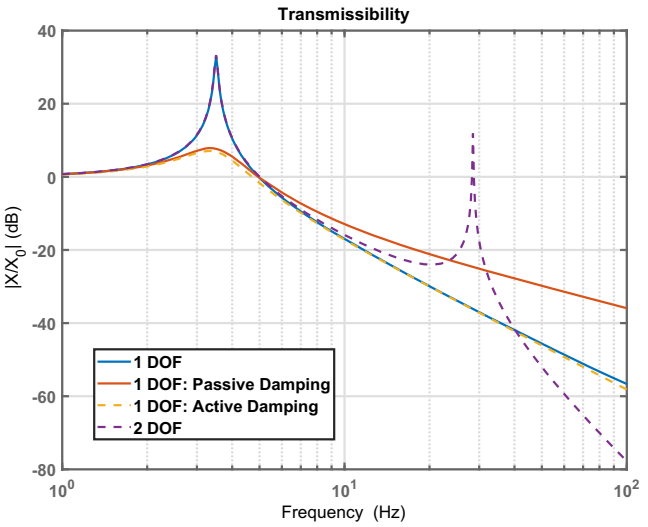

Fig. 1 Effect on the transmissibility of modifying the characteristics of a 1-DOF system.

$$Q = 1/2\xi \tag{2}$$

It is seen that the mechanical disturbances are filtered at frequencies above the resonance, with the transmissibility curve asymptotically rolling off at −40 dB/decade of frequency. Implementing multiple layers of isolation in series improves the roll-off of transmissibility; e.g., a two-degree-of-freedom (2-DOF) system shows a decrease of transmissibility of −80 dB/decade.

More flexible suspensions, i.e., with a lower natural frequency, show a transmissibility curve shifted to the left, broadening the frequency range of isolation and achieving a deeper isolation at a certain frequency. The caveat is that, at the resonance frequency of the suspension, an amplification of the disturbances occurs. Moreover, low resonance frequencies exhibit an increased displacement of the suspension for a certain acceleration input, and this imposes a practical lower limit to their resonant frequencies. The amplification occurring at the resonance frequency can be very detrimental to many applications, so there is often a need to curb it. Pistons flowing through viscous fluids are very effective in adding damping and limiting the peaks of transmissibility occurring at the suspension resonance, but these require a complex implementation and they also produce a degradation of the roll-off and therefore the isolation, as illustrated in Fig. 1. Alternatively, viscoelastic materials such as elastomers still provide a significant curbing of the resonant response while producing a less severe loss of isolation at the higher frequencies [18].

The big advantage of active isolation systems resides on their capability to very effectively limiting the amplification at the resonance, without affecting the roll-off of transmissibility [19]. As a result, the resonant frequencies of the isolation system can be decreased for enhancing isolation, without producing an increase in the displacements of the suspension modes. However, the better performances shown by active isolation systems come at the cost of added complexity in the form of sensors, actuators, the required control electronics and power supplies.

It must be noted that the description given above of isolation systems is idealized in that only the resonances of the suspension have been taken into account. In practice, secondary resonances of the interface and support structures are inherently present and, as will be seen in the next section, can significantly compromise the isolation performance.

B. Vibration Isolation Systems for Reaction Wheels

The extreme pointing stability required by the Hubble Space Telescope demanded that the disturbances generated by its reaction wheels be mitigated by supporting them on isolation mounts. Each of the three mounts consists of a pair of dampers involving springs and viscous fluid and are mounted parallel to the axis of spinning of the wheels [20,21].

Alternatively, isolation suspensions can be implemented by means of elastomeric mounts, which have a simpler design and preserve better the high-frequency isolation than viscous fluid dampers. Carte [22,23] describes such a concept developed for isolating the disturbances of the reaction wheels of the MTG satellites, and that rely on three elastomeric mounts tuned in stiffness and damping, and position with relation to the centre of gravity of the reaction wheel. These were qualified and embarked for flight, and the reported axial transmissibility consists of −40 dB of isolation at 200 Hz, but come at the cost of an amplification of 20 dB at the resonance frequency of 15 Hz of the suspension mode.

As an alternative to the elastomeric mounts, a suspension formed by washers made of a shape-memory-alloy metallic mesh has been proposed by Kwon et al [24]. Results are reported for a microvibration test on a shaker, putting in evidence a highly damped suspension mode at 20 Hz. A less-steep roll-off results in an isolation of −27 dB at 200 Hz and about −47 dB at 800 Hz, which is nonetheless very broadband, before the isolation is lost due to secondary resonances.

Interesting concepts of suspensions based on flexures with elaborate geometries have also been proposed and analyzed (one fully three-dimensional by Kamesh et al. [25]), while Wei et al. [26]

propose an in-plane two-dimensional flexure and predict by analysis its performances in isolating the radial disturbances generated by a reaction wheel.

Isolation platforms with the form of a hexapod allow independent authority over all six degrees of freedom. In the concept of the Stewart [27] platform, two plates corresponding to the noisy and quiet sides are interconnected by six struts forming the edges of a cube and therefore orthogonally connected. This results in a compact configuration, minimizes the interaction between the struts, and allows for applying an identical design for the six struts and a decentralized control in the case of active suspensions. Several concepts of isolating hexapod platforms have been proposed, both passive [28–30] and active [31–35].

A passive hexapod isolation platform has been successfully flown in the NASA Chandra X-Ray Space Telescope [28]. The suspension is implemented by means of titanium slotted springs, bonded with viscoelastic material. Transmissibilities were published for the three translational directions, showing a suspension mode at 10 Hz with an amplification of 20 dB, followed by a roll-off with a maximum experimental isolation of −18 dB at 100 Hz, which is then lost at increasing frequencies due to presence of secondary resonances [36].

This same design of isolation platform was then installed onboard the James Webb Space Telescope [2]. However, in this mission, microvibrations are further reduced by installing a second layer of isolation, i.e., by supporting the optical telescope element on a very flexible truss bonded with visco-elastic material.

More complex designs for the hexapod struts have evolved in the meanwhile. Honeywell further developed the fully passive D-strut viscous dampers operating on the Hubble Space Telescope [21], by adding voice coils moving in the direction of active and hybrid concepts. Davis et al. [32] report the uni-axial testing of such a second-generation D-strut, in which an actively controlled strut exhibits a suspension mode at 15 Hz, with negligible amplification, followed by a sustained −20 dB isolation between 20 and 200 Hz, which improves to −60 dB at 800 Hz.

A similar active concept is described by Lee et al. in [37], further implementing force sensors. The performance of a full hexapod platform was experimentally characterized with the operation of a reaction wheel. The system exhibits suspension modes at 10 Hz, and an isolation of −40 dB is achieved at 100 Hz.

Furthermore, novel concepts of active struts have emerged more recently, in which the dampers with viscous fluids have been replaced by dampers based on electromagnetic shunting (via voice coils) with negative resistance synthesized with electrical circuits [34,35]. Test results are reported for a hexapod with suspension modes at 2–3 Hz. Introduction of multiple flexible elements in series with masses results in a 2-DOF system with a roll-off of the transmissibility of −80 dB/decade landing on an isolation of −60 dB at 100 Hz. However, due to the presence of secondary resonances, in particular bending modes of the struts, the isolation reverts to −20 dB at 200 Hz and remains compromised above those frequencies.

It becomes clear from studying the available literature that the performance of a given isolation system is dependent on the characteristics of the roll-off of the transmissibility after the system's resonance. The main factors affecting this roll-off are its starting point, given by the resonance frequency of the system; its slope, dependent on the damping of the system where lower damping results in a steeper slope; and the appearance of secondary resonances rising from local deformation modes in the transmission path of the disturbances. To maximize the isolation performance of a system it is therefore important for it to have a low resonance frequency, low damping, and no secondary resonances in the frequency band of interest for the isolation. However, a low value of damping required to preserve the high-frequency isolation results in a high amplification of the disturbances occurring at the resonance frequency of the isolator. To tackle this issue, active control, in the form of relative velocity feedback, is applied at frequencies around the suspension resonance.

The objective in the development of the active platform presented in this paper is to improve the isolation performances with relation to those published in the literature available and presented above in the review of the state-of-the-art, while maintaining a simple enough configuration to make the isolator attractive to be embarked on a satellite. The active platform presents a high-isolation factor due its low resonance frequency and absence of local deformation modes up to 500 Hz, achieving 60 dB of reduction in the transmitted forces at 130 Hz, with a maximum recorded reduction of 65 dB at 270 Hz. Active control is used to damp the main suspension modes, reducing the amplification at their corresponding frequencies.

This paper summarizes the development and testing of a multi-DOF active isolator platform for microvibrations and is organized as follows:

- Section I is the introduction.
- Section II describes the targets specified to the platform and the design choices driven by them.
- Section III shows the results from the experimental validation carried out with both a dummy and a real disturbance source, along with the assessment of the performances achieved.
- Section IV sums up the results, and discusses potential future developments for the platform concept.

II. Isolator Design and Analysis

A. Brief Description of the Isolator

The isolator consists of two plates, one interfacing the reaction wheel (source plate) and another one interfacing the satellite (base plate). These two plates are connected by six struts in a Stewart platform configuration. To avoid the rise of secondary resonances coming from complex structures like joints and guiding mechanisms in the struts, frameless voice-coil actuators are installed in each strut. To support the top plate, a set of six springs, distributed symmetrically in pairs around the platform, has been designed. The resonance frequency of the suspended system has been targeted at 5 Hz, since it is an early starting point for the isolation, but not low enough to interfere with the attitude control system of the spacecraft. The isolator is depicted in Fig. 2.

For this prototype, aluminum has been selected as the main material, since it allows to meet the above requirements, presents easy machinability, and has a strong aerospace heritage. Practical implementations in the further development of this system is to investigate the use of carbon-fiber-reinforced polymer (CFRP) as the main structural material in order to make it more mass efficient.

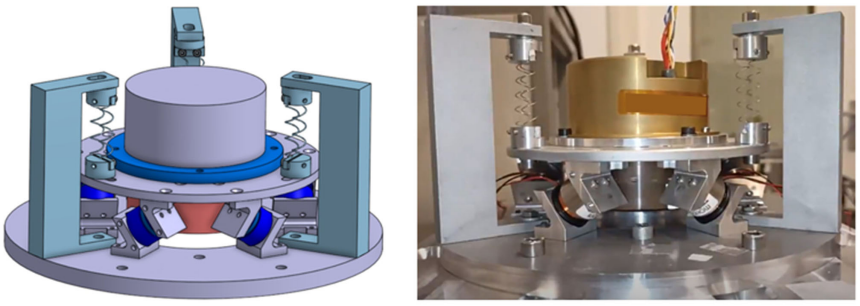

a) b)

Fig. 2 a) The 3D model of the isolator with the actuators highlighted in dark blue; b) isolator with reaction wheel in operating conditions.

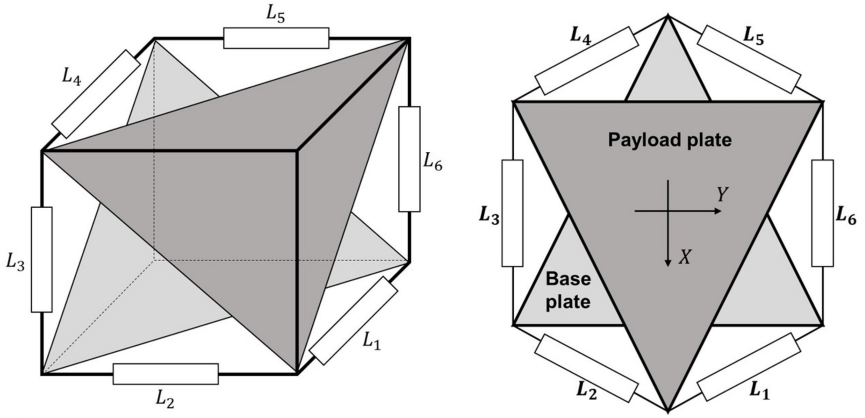

Fig. 3 Schematic views of the cubic configuration of a Stewart platform: a) isometric view; b) top view.

B. Stewart Platform

There are two key aspects to the design of the struts: the first one being the disposition of each strut with respect to the payload and base plate, and the second one being the connections in the struts.

For this application, a cubic configuration of the struts is selected. This layout presents several advantages when performing active control that have been covered in literature, among which are uniformity of control capability in all directions and minimum cross-coupling among actuators [38]. To obtain a cubic configuration, two parallel planes are sliced from a cube as shown in Fig. 3, each one representing one plate of the platform, where the lines marked by L form the struts.

The equation of motion of the suspended part of the Stewart platform can be written according to [33,38–40] as

$$M\ddot{X} + C_d\dot{X} + KX = F_{vc} + F_{rw} + KW \tag{3}$$

where

X = vector describing the position and rotations of the payload plate of the Stewart platform in Cartesian coordinates = $[x, y, z, \theta, \phi, \gamma]$;

W = vector describing the position and rotation of the base of the Stewart platform in Cartesian coordinates;

M = matrix of mass and inertia associated to the kinetic energy = diag$[m; m; m; I_\theta; I_\phi; I_\psi]$;

K = stiffness coupling between the two surfaces via the springs of the suspension;

C_d = matrix representing the damping of the system;

F_{rw} = forces and moments applied by the reaction wheel; and

F_{vc} = forces and moments applied by the voice coils (since the voice coils are frameless, they can be expressed as $F_{\text{vc}} = J^T f$, in terms of the axial forces generated by the voice coils by means of the Jacobian matrix).

The kinematic relationship J between the motion in the direction of each strut q (a vector consisting of six elements, one for each strut), and of a point at the center of mass of the source plate X, is shown in Eq. (4).

$$q = JX \tag{4}$$

To be solved, the equation of motion can be written in the state-space form:

$$\dot{x} = Ax + Bu \tag{5}$$

$$y = Cx + Du \tag{6}$$

by defining the state variables and inputs, respectively, as $x = [X; \dot{X}]$ and $u = [W; F_{rw}; f]$, the matrices can be written as

$$A = \begin{bmatrix} 0_{[6\times6]} & I_{[6\times6]} \\ -K/M & -C_d/M \end{bmatrix}; B = \begin{bmatrix} 0_{[6\times6]} & 0_{[6\times6]} & 0_{[6\times6]} \\ K/M & 1/M & kJ^T/M \end{bmatrix};$$
$$C = \begin{bmatrix} I_{[6\times6]} & I_{[6\times6]} \end{bmatrix}; D = [0] \tag{7}$$

in which the outputs become the positions and rotations of the Stewart platform and its time derivatives.

The matrices above will then allow the creation of a state-space object in MATLAB, where a controller, as implemented in this paper, can be simulated by making $f = H(s)JX$, with $H(s)$ described in Sec. II.D. The tuning and simulation of the Stewart platform can then be performed via the *sisotool* and *feedback* commands in MATLAB.

Figure 4 shows example diagrams of a guided voice-coil actuator with a flexure and a frameless voice coil. In guided actuators, the guiding flexure mechanically links the stationary and moving sections of the actuator, becoming part of the transmission path of

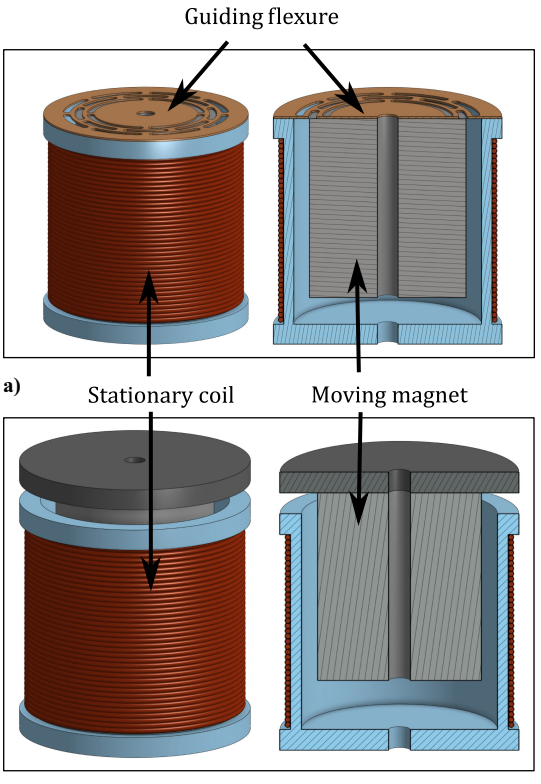

Fig. 4 Full view and cross section of example models of a) a guided voice-coil actuator, and b) a frameless voice-coil actuator.

disturbances. These flexures are typically made of thin, slotted metal plates that ensure a colinear displacement between the magnet and the coil. Made to be compliant, the stiffness in these flexures is low and therefore present local deformation modes at low frequency that give rise to secondary resonances in the transmission path, degrading the isolation. For this reason, frameless voice-coil actuators have been chosen, eliminating any mechanical connection in the actuators and facilitating the design of a clean transmission path for the disturbances. The selected voice coils also present a larger clearance than is typical for their size to accommodate for the relative motion of the platform in all six degrees of freedom.

The actuator supports have been designed to be able to accommodate the voice coils, while having space for extra accelerometers to be placed co-axially on the opposite face and used for monitoring during these on-ground tests. The same support has been designed for all actuators to have good symmetry in the isolator.

C. Supporting Springs

The lack of a mechanical connection in the struts rises the need to include additional supports in the platform. To this end, three sets of springs are symmetrically distributed around the platform as shown in Fig. 5.

The spring's characteristics, material, number of turns, spring wire diameter, and spring diameter have been specifically chosen for two purposes: the first one is to provide the required stiffness of 160 N/m in each spring to, together with the suspended mass, result in an overall suspension resonance of 5 Hz; the second one is to not present local deformation modes (internal resonances in the spring where the coils deform independently) below 500 Hz. These two goals have been accomplished by fulfilling Eqs. (8) and (9), where k is the spring stiffness, G is the material's shear modulus, ρ is the density of the material, d is the spring wire diameter, D is the spring diameter, N_a is the number of turns in the spring, and f_{res} is the resonance frequency of the first local deformation mode.

$$k = \frac{Gd^4}{8D^3N_a} \tag{8}$$

$$f_{\text{res}} = \frac{d}{2\pi D^2 N_a}\sqrt{\frac{G}{2\rho}} \tag{9}$$

The values chosen for the above variables in order to fulfill the stiffness and internal resonances conditions are shown in Table 1 and resulted in a slender spring susceptible to buckling when undergoing large amounts of compression. The springs are therefore mounted in tension.

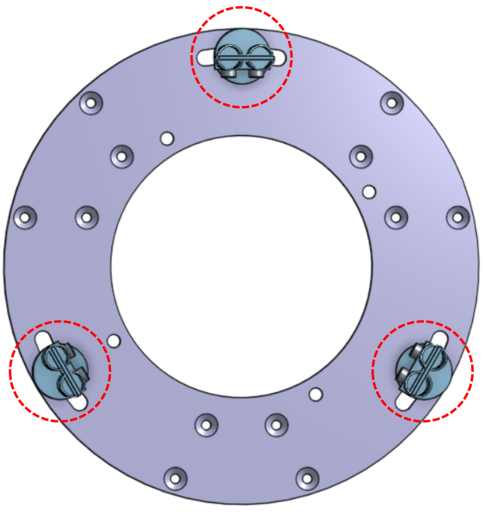

Fig. 5 View of source plate indicating the spring locations.

Table 1 Parameters chosen for the design of the springs in spring steel EN-10270-3 Type 302

Material properties	
Shear modulus (G), GPa	73
Material density (ρ), kg/m^3	7920
Geometric properties	
Spring diameter (D), mm	7.2
Number of turns (N_a)	4
Spring wire diameter (d), mm	0.4

To mount the springs in tension, a bracket has been designed with no local modes under 500 Hz on which the spring clamps can be attached. The spring clamps are designed with adjustable spacing between the bracket and the clamp, enabling fine-tuning of the static position of the platform. The horizontal position of the springs can be adjusted by changing their mounting position on the slots located in the source plate (shown in Fig. 5).

The on-ground testing configuration consists of two springs per spring clamp per bracket, symmetrically spaced around the platform. However, once the payload enters a zero-g environment, the weight of the platform will no longer be affecting the springs, and the static position of the source plate will change. This change in static position has been accounted for, and can be mitigated by switching one of the springs in each pair from connecting the source plate to the brackets, to connecting the source plate to the base plate, as shown in Fig. 6d. By connecting the springs in an opposing way, the tension forces in the springs are compensated, and the source plate remains at its optimal position. The on-ground testing configuration has been used to produce the results showcased in this document.

The performance of each spring pair has been individually evaluated before mounting on the platform. Each spring has been tested of an assembly consisting of two springs in parallel held by one spring clamp at each end. Two different setups have been used.

The goal of the first setup is to verify the stiffness of the three spring assemblies, represented by k_1, k_2, and k_3. The setup consists of a static force sensor attached to one end of each spring assembly, and a translation stage attached to the other. Starting from the spring's natural length of 19 mm, a set deformation can be introduced in each spring assembly, and the corresponding force measured, allowing for accurate calculation of the stiffness of the spring assembly throughout the range of deformation of its constituting springs. Figure 7 shows a picture of this setup.

Figure 8 shows that the behavior of the springs is linear in the tested regime, and the stiffness of each spring assembly is very close, with a maximum difference of 7 N/m found between k_1 and k_3. These results correspond well with the simulations done during the design phase of each individual spring, where a stiffness of 160 N/m per spring was targeted, resulting in 320 N/m for each assembly of two springs in parallel.

The goal of the second setup was to check for local deformation modes in each spring assembly at undesirable frequencies. Force sensors are connected to each end of the spring assembly, where one is fixed and the other one is attached to an electrodynamic shaker. This arrangement allows introducing a broadband disturbance in the system, exciting any resonances present in the frequency range of interest that will appear in the transfer function between the measurements of the two force sensors. Figure 9 shows a picture of this setup.

The results obtained from the setup in Fig. 9 are shown in Fig. 10. A resonance can be seen at low frequency corresponding to the moving mass of the shaker, followed by a −40 dB/decade roll-off, with the resonances of the test setup appearing at 200 and 315 Hz. The behavior of each spring pair is identical except the spring assembly "Spring pair–Bracket 3" in the frequency band of 280–300 Hz, where a minor difference in mounting has been identified as the cause. The resonances shown at 200 and 315 Hz originate in the shaker, whereas the resonances shown in the frequency range of 500–700 Hz are a

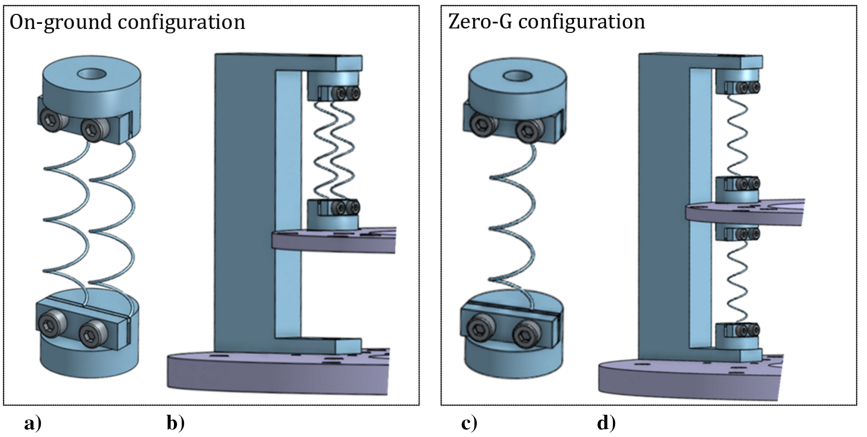

Fig. 6 View of different suspension system configurations: a, b) on-ground; c, d) zero-*g* clamp.

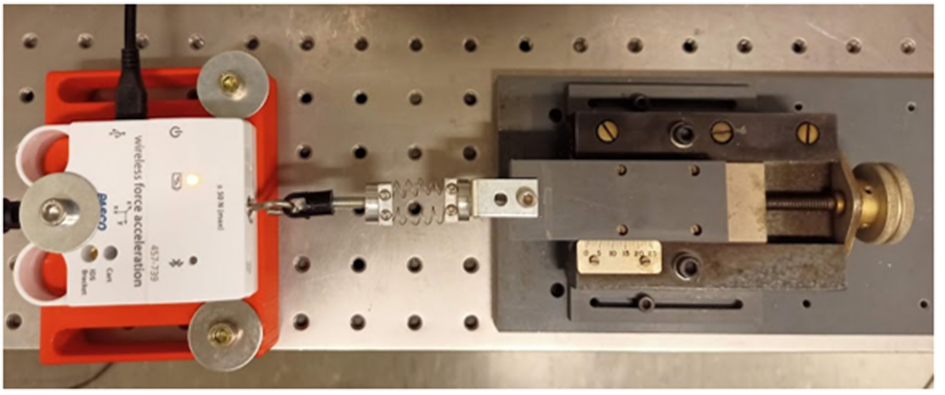

Fig. 7 Test setup to evaluate the spring's stiffness.

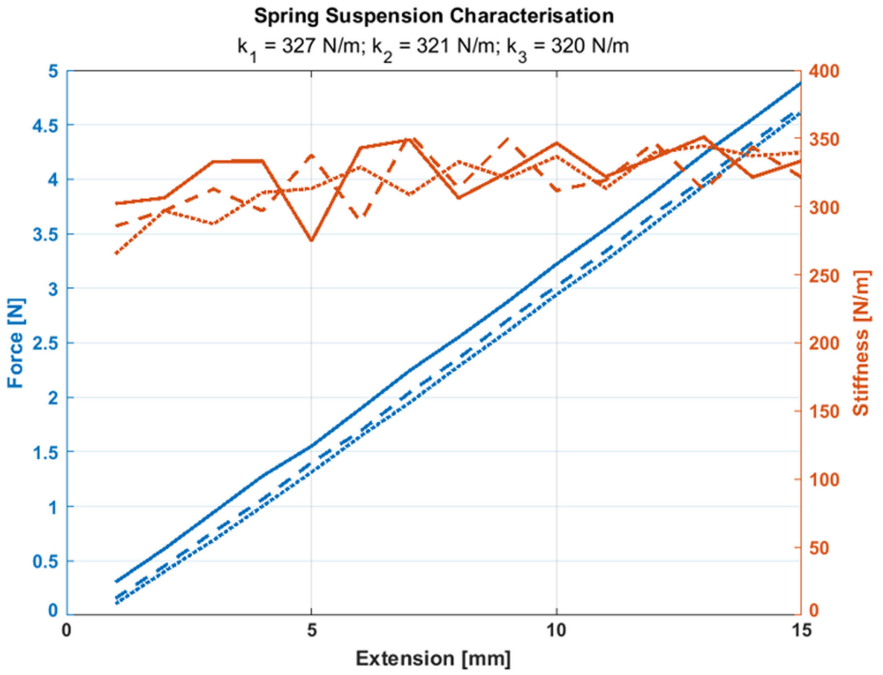

Fig. 8 Force (blue) and stiffness (red) of each spring assembly consisting of two springs in parallel as a function of the induced extension.

combination of the internal resonances of the springs and resonances of the setup.

D. Active Control

To avoid the magnification of disturbances at the resonance frequencies of the isolator, active control is used. The relative velocity between the source and base plates in the axis of each actuator is used as an input for the controller. The voltage drop V_m across the terminals of a voice-coil actuator is a function of the current i moving through it, and the relative velocity v between the actuator's stationary and moving sections [41]. This equation can be written as

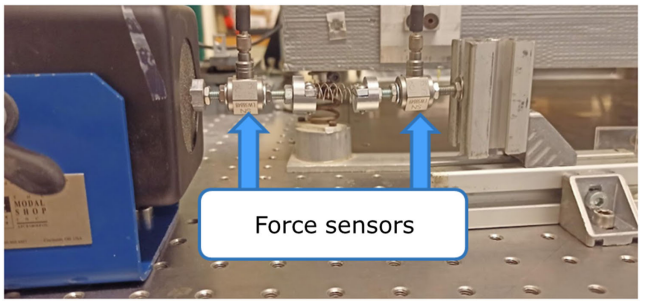

Fig. 9 Test setup to evaluate the dynamics of each spring assembly.

$$V_m = Ri + L\frac{di}{dt} + T_{\text{em}}v \tag{10}$$

where T_{em} is the electromechanical coupling coefficient, and R and L are the coil's resistance and inductance. This equation can be rearranged to show how to obtain the relative velocity from the actuator's properties and the measured voltage drop and current:

$$v = \frac{V_m - Ri - L(di/dt)}{T_{\text{em}}} \tag{11}$$

Computing the relative velocity from Eq. (11) enables to use the voice coils as both actuators and sensors. There are several advantages of using the actuators in self-sensing mode. Each sensor–actuator pair in a self-sensing setup is collocated by definition, since the actuator and the sensor are the same element, and therefore act and measure on the same location. Collocated sensor–actuator pairs present alternating poles and zeros in their open-loop transfer function, as demonstrated in [19] and is observed in the experimental transfer function. The phase shift caused by each pole is compensated by the following zero, avoiding phase cumulations and locking the phase between −180 and 180°, thus ensuring the stability of the system. The overall weight, complexity, power draw, and possible failure points of the system are reduced by removing additional sensors. A transmission path for disturbances between the source plate and the base plate is removed by eliminating the cable that would be connected to any sensor placed on the source plate. Figure 11 shows a block diagram with the control architec-

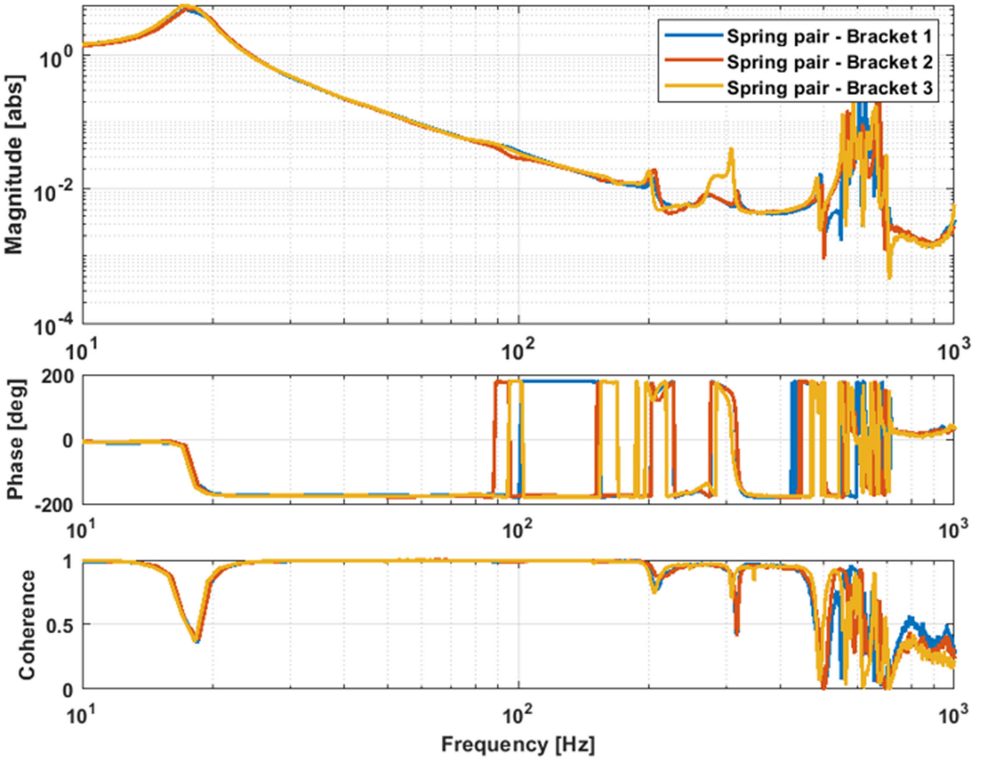

Fig. 10 Force transmissibility, phase, and coherence for each spring assembly pair.

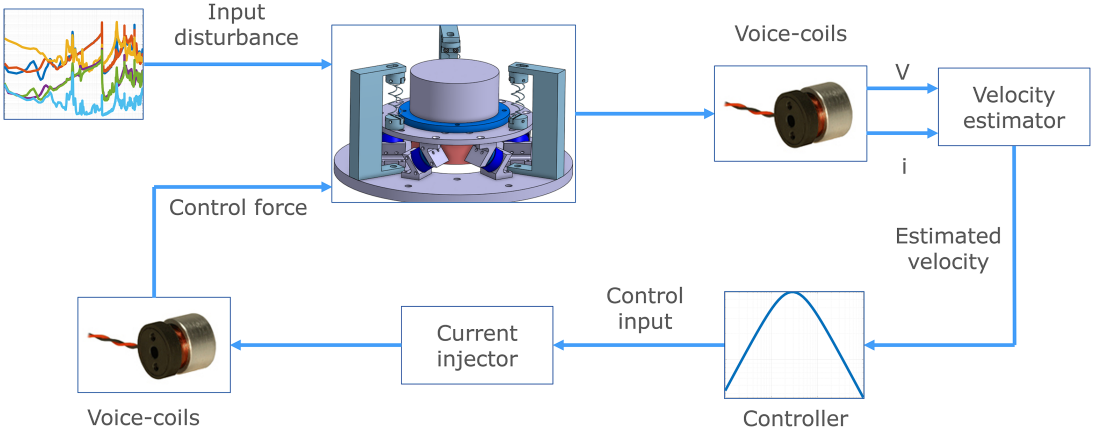

Fig. 11 Block diagram representation of the active control loop.

ture. Currently the measured voltage and current signals are connected to a DSpace MicrolabBox system where the controller is implemented, and the resulting signal is sent to a current injector feeding the actuators. This system can be implemented on an analogue circuit to reduce its size and weight for its in-flight implementation.

The open-loop transfer function for one of the sensor–actuator pairs (all of them are equivalent) can be seen in Fig. 12. This curve has

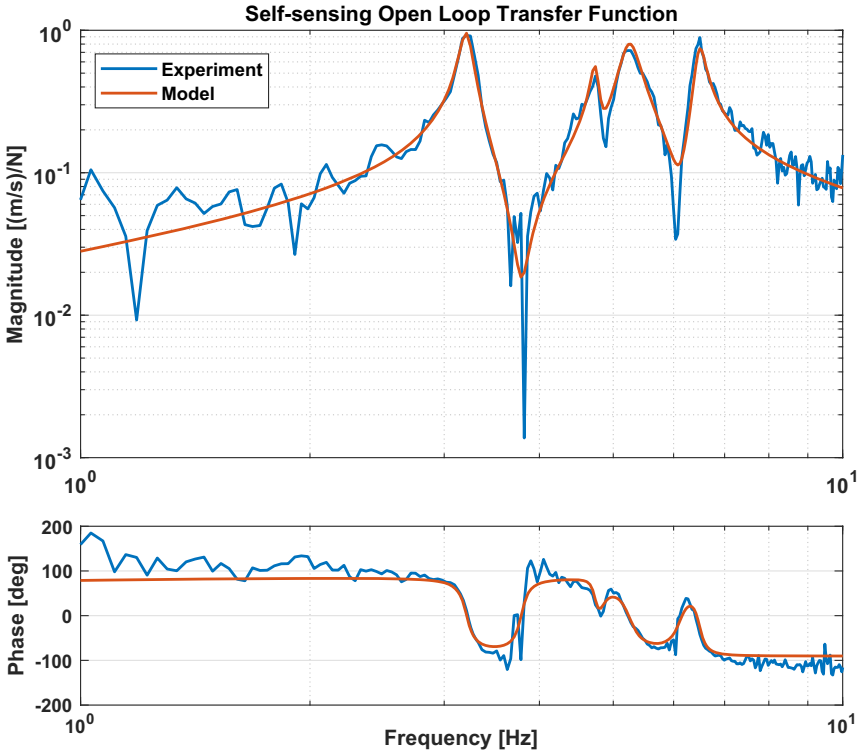

Fig. 12 Open-loop transfer function between the self-sensed velocity and the force injected in one actuator showcasing alternating poles and zeroes.

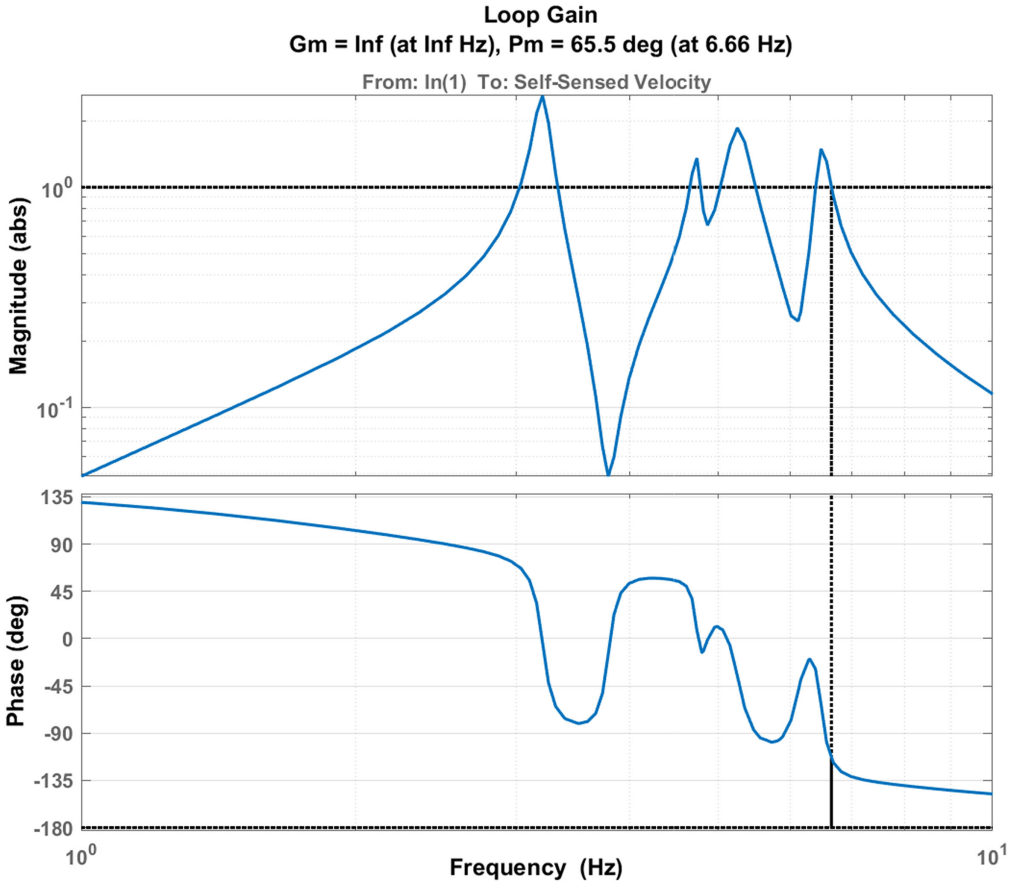

Fig. 13 Loop gain and stability margins of the system.

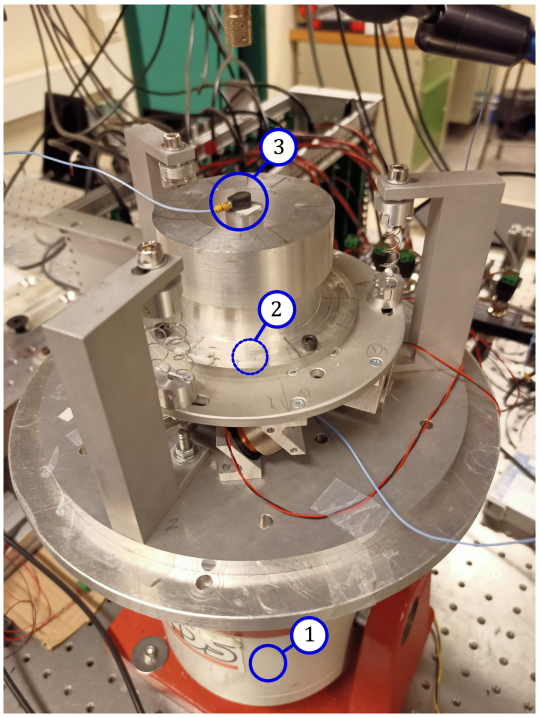

Fig. 14 Experimental setup at ULB to verify the platform's passive and active isolation performance.

been obtained by injecting Gaussian white noise in one voice coil while measuring the relative velocity of the excited voice coil through self-sensing.

The *fitfrd* function from MATLAB is used to obtain the model curve. The quality of fit is quantified in terms of mean-squared error (MSE), which ranked extremely low compared to the range of fitted values. The mathematical model of the open-loop transfer function allows to design a controller, by checking its stability through the loop gain. A negative derivative feedback (NDF) [42] controller is considered for damping the targeted mode of the system. NDF is a band-pass filter that cuts off the control action far from the natural frequencies associated with the controlled modes, reducing the spillover effect. As a bandpass filter it can effectively control the lower and higher frequency disturbances. An approach for an optimal design of NDF controller to implement on collocated systems is used [43]. The fitted model is considered and a mode of this system is targeted to damp. The maximum damping method is used to determine the suitable candidates for the controller's constants in order to be dependent based on closed-loop damping parameter. Afterward the H_2 method is utilized to select the optimal values among the identified candidates. The results show that NDF can easily damp a targeted mode impactfully. The designed controller is presented in Eq. (12), where g is the selected gain. The loop gain for this controller, obtained by multiplying the open-loop transfer function and the controller, and the corresponding stability limits are presented in Fig. 13.

$$H(s) = g\frac{s}{s + (2\pi * 2.4)}\frac{1}{s + (2\pi * 3.4)} \tag{12}$$

The experimental results obtained with this controller are presented in Sec. III.A.

III. Isolator Performance

The isolation platform was tested in the axial DOF at the Bio-Electro and Mechanical Systems Laboratory at Unviersité Libre de Bruxelles (ULB), which allowed for tuning of the active control parameters. The setup was then moved to the Mechanisms Laboratory at the European

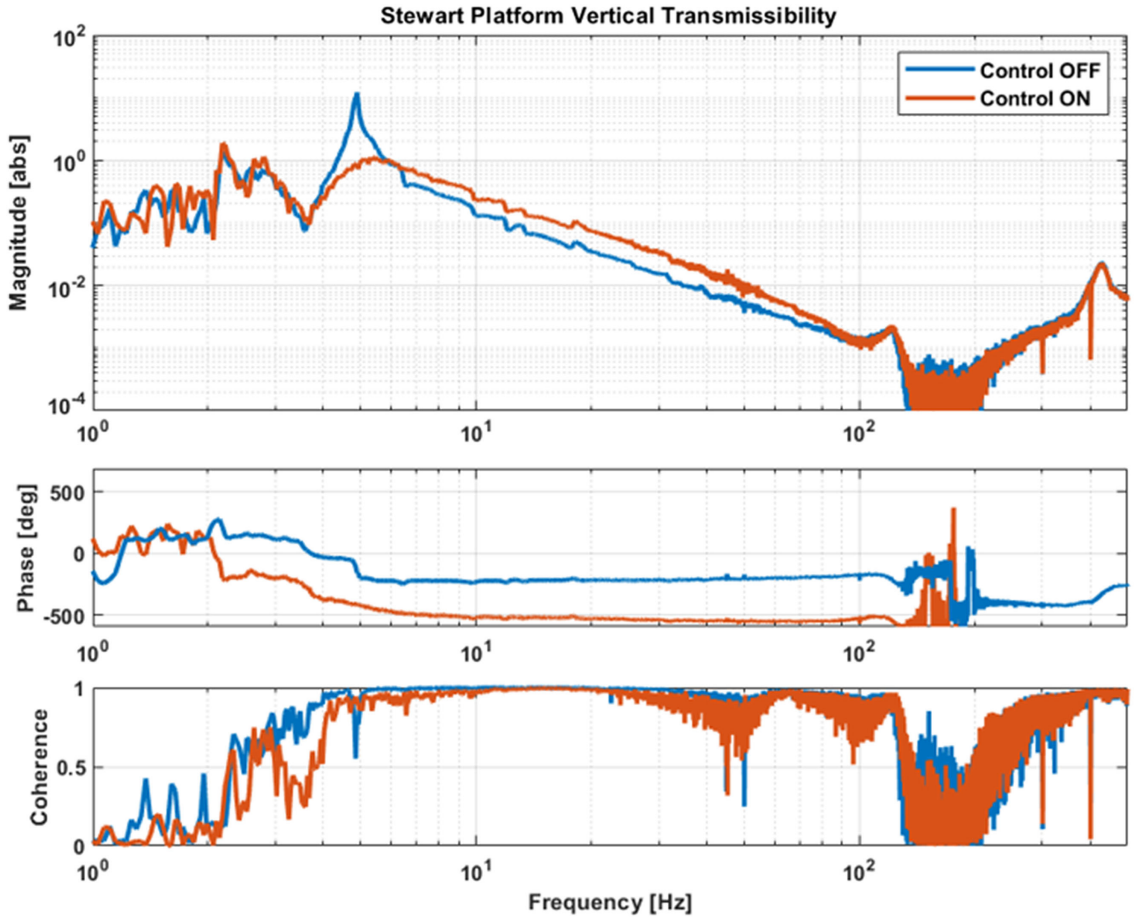

Fig. 15 Experimental transmissibility of the isolator in axial direction. Attaining 60 dB of isolation at 100 Hz.

Space Research and Technology Centre (ESTEC) site of the European Space Agency for testing with a test model of a reaction wheel that provided a disturbance in all six degrees of freedom simultaneously.

A. Single-DOF Experimental Characterization

The isolation performance in axial direction was characterized in terms of the motion transmissibility between the base and source plates. For this purpose, the platform was mounted on an electrodynamic shaker (labeled 1 in Fig. 14), and subjected to a broadband base vibration excitation, as illustrated in Fig. 14. A dummy representative of the mass and inertia of the test reaction wheel that will be used later was mounted on the top plate (labeled 2 in Fig. 14). A bias current was applied to the voice coils to precisely locate the suspended platform at its optimal position where the clearance between the coils and the magnets is maximized.

Two accelerometers were placed at the center of both the source (labeled 3 in Fig. 14) and base plates in order to compute the motion

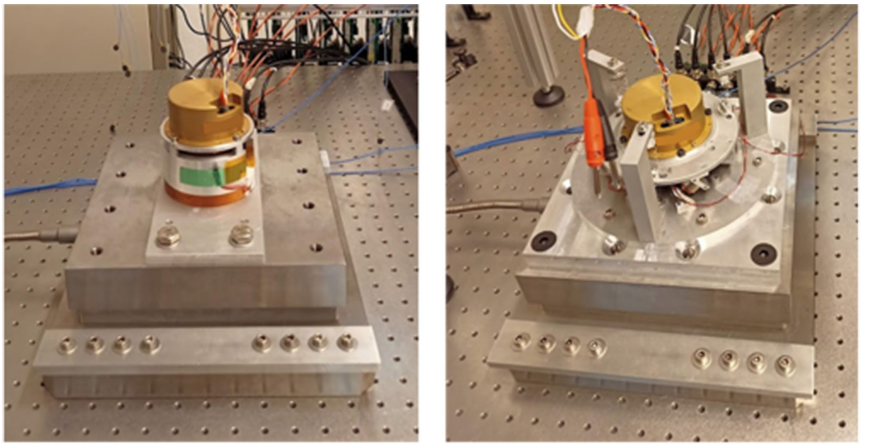

a) b)

Fig. 16 Test configurations to compute the force transmissibility of the isolator. a) Hard-mounted configuration used as reference. b) Isolated configuration used for measuring disturbances with isolation platform.

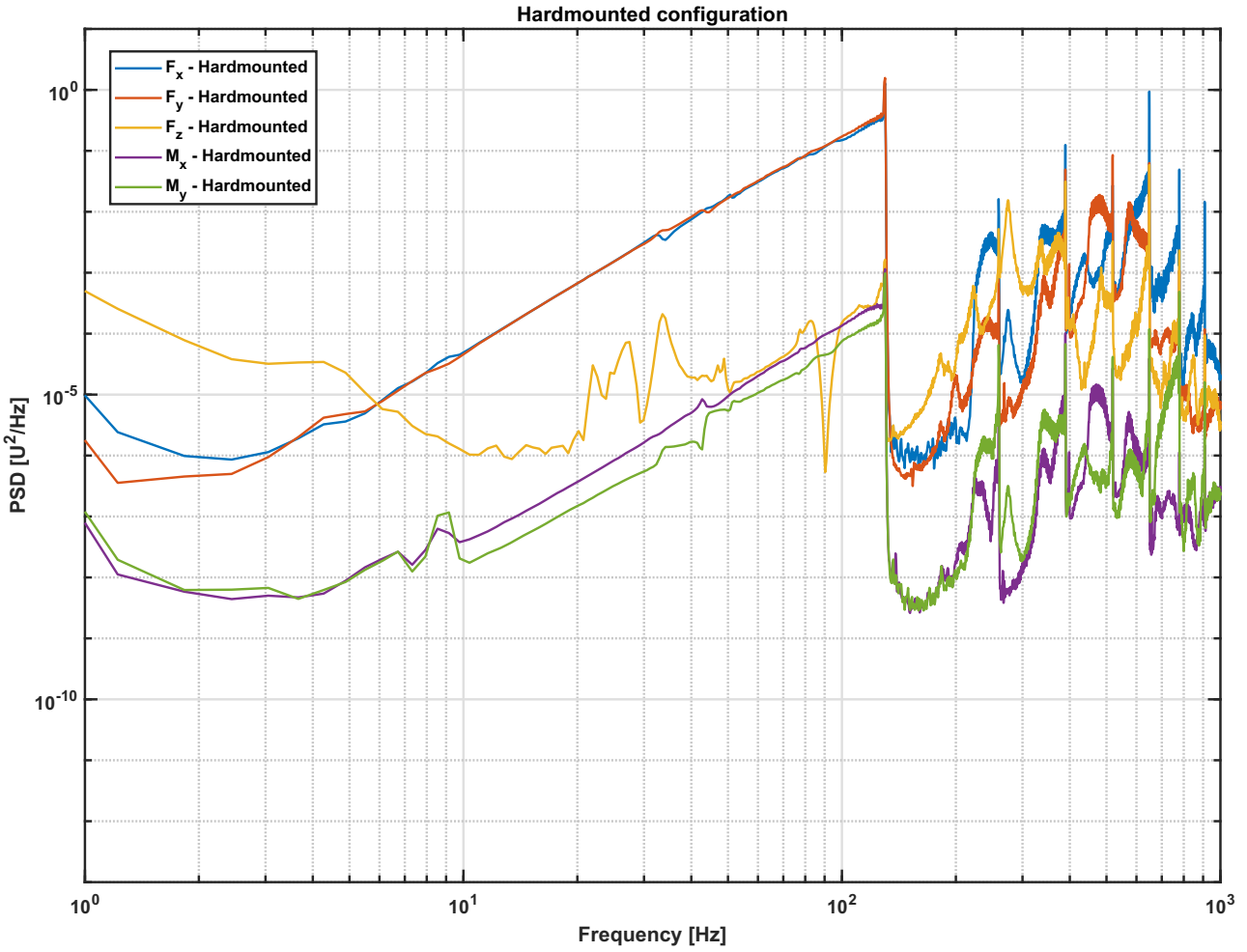

Fig. 17 Power spectral density of forces (where the unit U = N) and moments (where the unit U = Nm). Unbalance can be seen in the slope from low frequency up to 130 Hz.

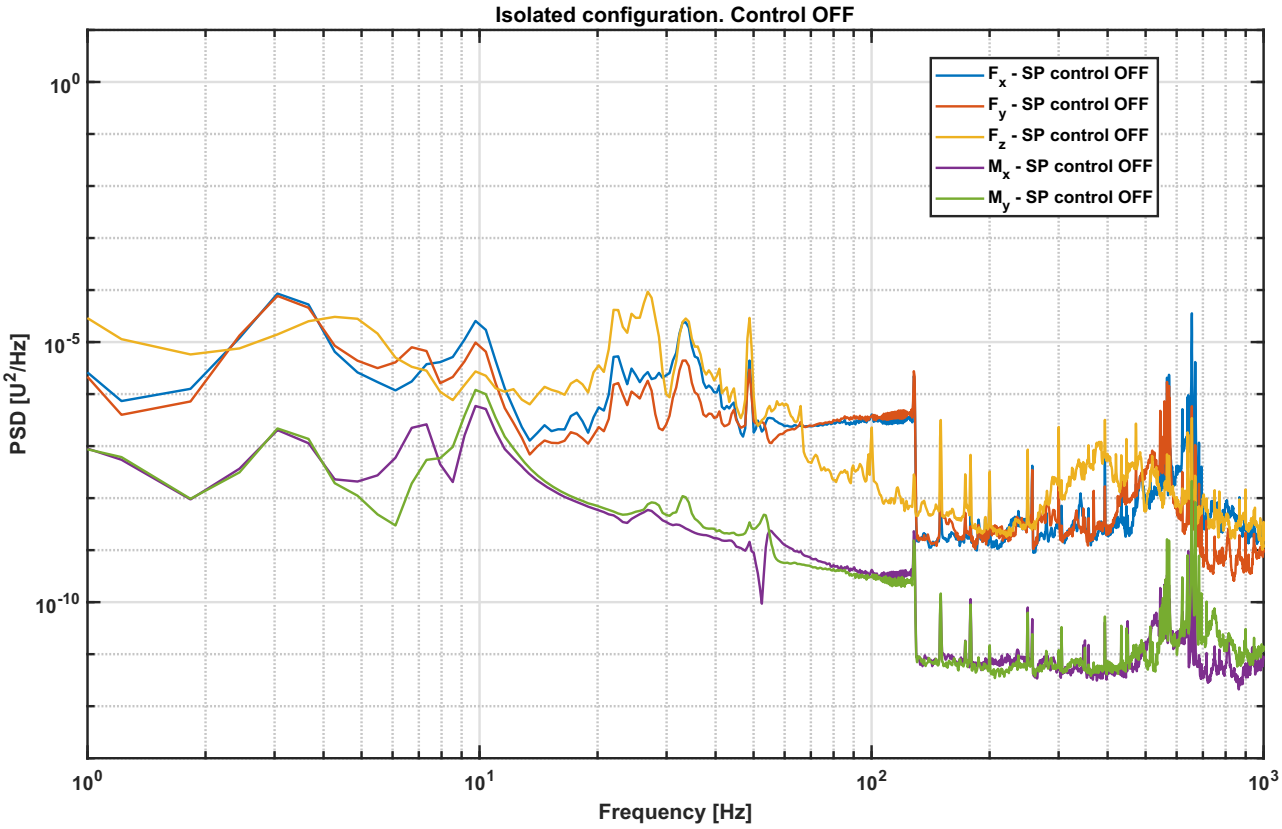

Fig. 18 Power spectral density of forces (where the unit U = N) and moments (where the unit U = Nm) with the reaction wheel mounted on the isolator. Control off. Isolator roll-off compensates unbalance.

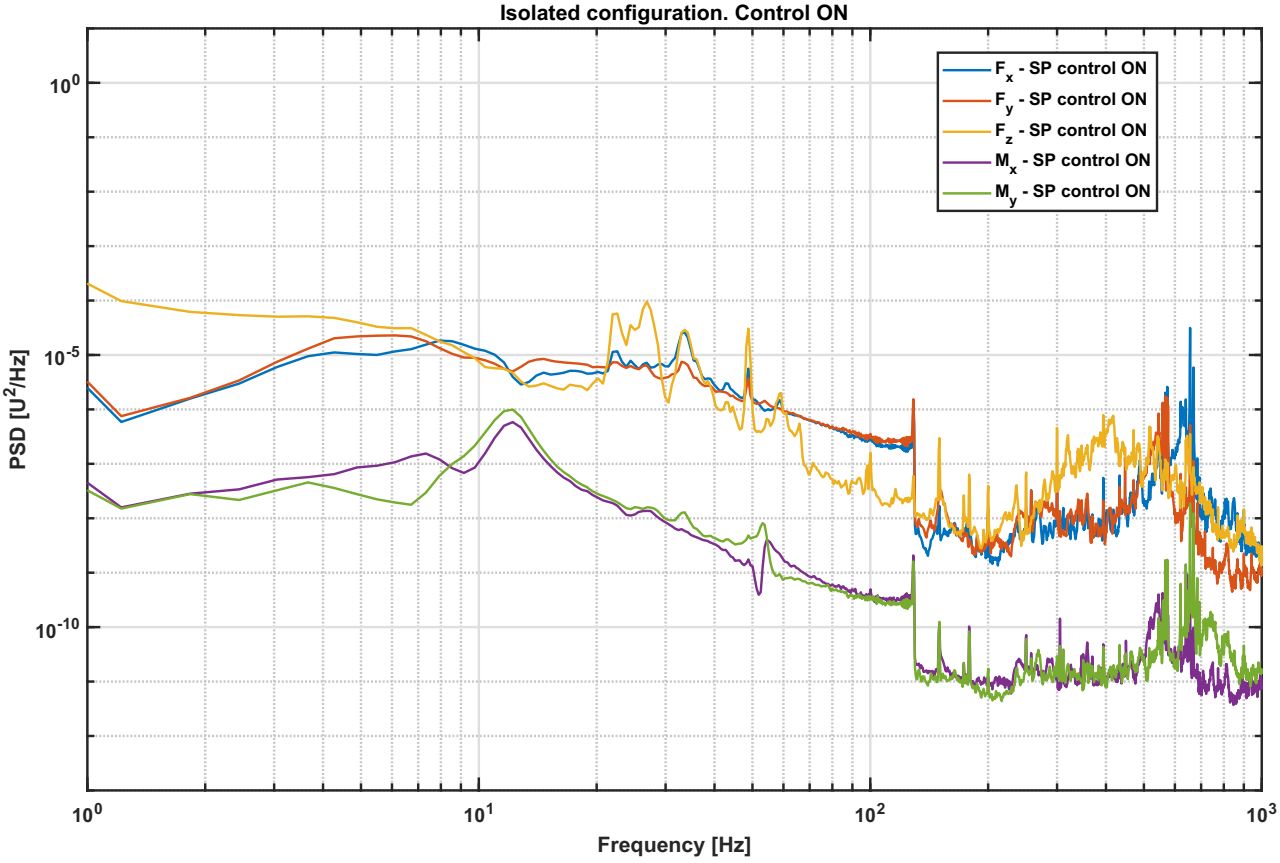

Fig. 19 Power spectral density of forces (where the unit U = N) and moments (where the unit U = Nm) with the reaction wheel mounted on the isolator. Control on. Damping of the low-frequency resonances is observed.

transmissibility of the system. Although the performance metric of interest is the force transmissibility, it can be shown that in systems without active control and systems with relative velocity control, the motion transmissibility and the force transmissibility of a system are equivalent; analytical proof is included in the Appendix. The resulting transmissibility can be found in Fig. 15.

A reduction of 60 dB in the transmitted motion (equivalent to the force) can be observed at 100 Hz for the active and passive cases. Switching the active control on produces the expected results of successfully damping the resonance, although with some loss of the isolation in the roll-off region. This degradation of the isolation is due to the increased damping in the system introduced by the active control. The drop in coherence below 5 Hz is due to the limited capability of the shaker in introducing excitations at such a low frequency. In the frequency band of 150–300 Hz, due to the high isolation factor of the platform, the disturbances reaching the accelerometer placed on the source plate are smaller than its resolution, leading to the sensor outputting noise. The resulting values seen in this frequency range cannot be regarded as reliable, and further investigation is necessary. However, this drop in coherence implies a performance of the isolation at these frequencies higher than the −60 dB seen at 100 Hz.

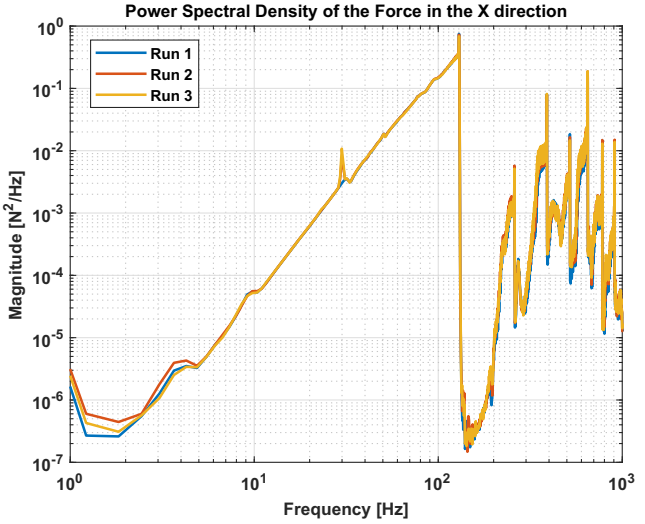

Fig. 20 Force PSD in the *X* direction for independent passive coast-downs, illustrating the repeatability of the disturbances created.

B. Multi-DOF Experimental Characterization

After the initial performance verification at ULB, the isolator is moved to the Mechanisms Laboratory at the ESTEC site of the European Space Agency, with the goal of installing a functional test model of a reaction wheel on the isolator that generated disturbances in the six degrees of freedom simultaneously. This test is representative of the isolating suspension's true operating conditions except for the presence of gravity.

A picture of the test setup is shown in Fig. 16. The test reaction wheel is mounted on the isolator, which is in turn bolted to a dynamometer, attached to the top of an optical table. The dynamometer used is a Kistler 9255A, which consists of two plates interfaced by four tri-axial piezoelectric force sensors at its corners. The outputs of these sensors and the knowledge of the distances between them allow the reconstruction of the disturbing forces and moments generated by the test paper.

The assessment of the performance of the isolator platform is carried out by computing the ratio between the force measured by the dynamometer while the reaction wheel is directly hard-mounted on it without the isolator (Fig. 16a), and the force measured by the dynamometer when the isolator is installed (Fig. 16b). The measured forces and moments for the corresponding configurations are shown in Fig. 17 for the hard-mounted case, and in Figs. 18 and 19 for the reaction wheel mounted on the isolator, with and without active control.

To achieve broadband excitation from the reaction wheel, in each test, the rotor was spun up to its maximum speed of 7800 rpm, then power was removed, and the forces and moments were recorded while it coasted down to a stop, taking an average of 300 s. The power spectral densities of the forces were computed for both cases. The force and moment transmissibility of the isolation platform was computed through Eq. (13), as proposed in [44]. This is justified, since a good repeatability of the measured disturbances was observed throughout different tests, for both with and without the presence of the isolator platform. As an example, Fig. 20 presents the results for the disturbance forces measured in the *X* direction in three different tests, for the case of the reaction wheel hard-mounted on the dynamometer.

$$|T_{\text{Force}}| = \frac{\sqrt{\text{PSD}_{\text{isolated}}}}{\sqrt{\text{PSD}_{\text{hardmounted}}}} \tag{13}$$

Figure 21a superimposes the disturbing forces measured along the *X* direction for different configurations, including the wheel hard-mounted on the dynamometer, the wheel mounted on the isolation platform with the active control ON and OFF, and a static wheel used as reference for background noise. The background noise dominates the measurements made with the isolation platform between 20 and 50 Hz and at multiple limited frequency bands above 130 Hz.

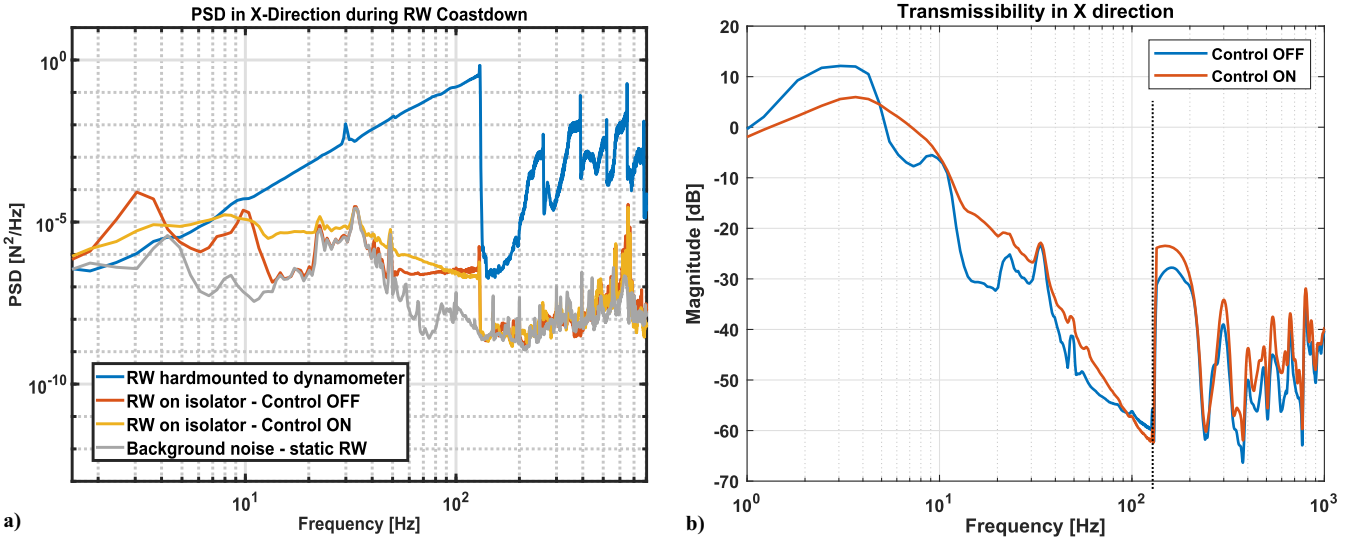

Fig. 21 a) Effect of background noise on measured signals; b) corresponding transmissibility with and without control, showcasing an increase at 130 Hz due to background noise.

The direct application of Eq. (13) to the F_x disturbance measurements from Fig. 21a is illustrated in Fig. 21b. It is worth noting that at 130 Hz an attenuation of −60 dB is achieved, while damping the suspension resonance at low frequency when using active control. By introducing damping into the system, the roll-off is degraded, resulting in the effect seen between the main resonance and 130 Hz. However, this effect is negligible if one considers the envelopes of the peaks between control ON and OFF, in this frequency band.

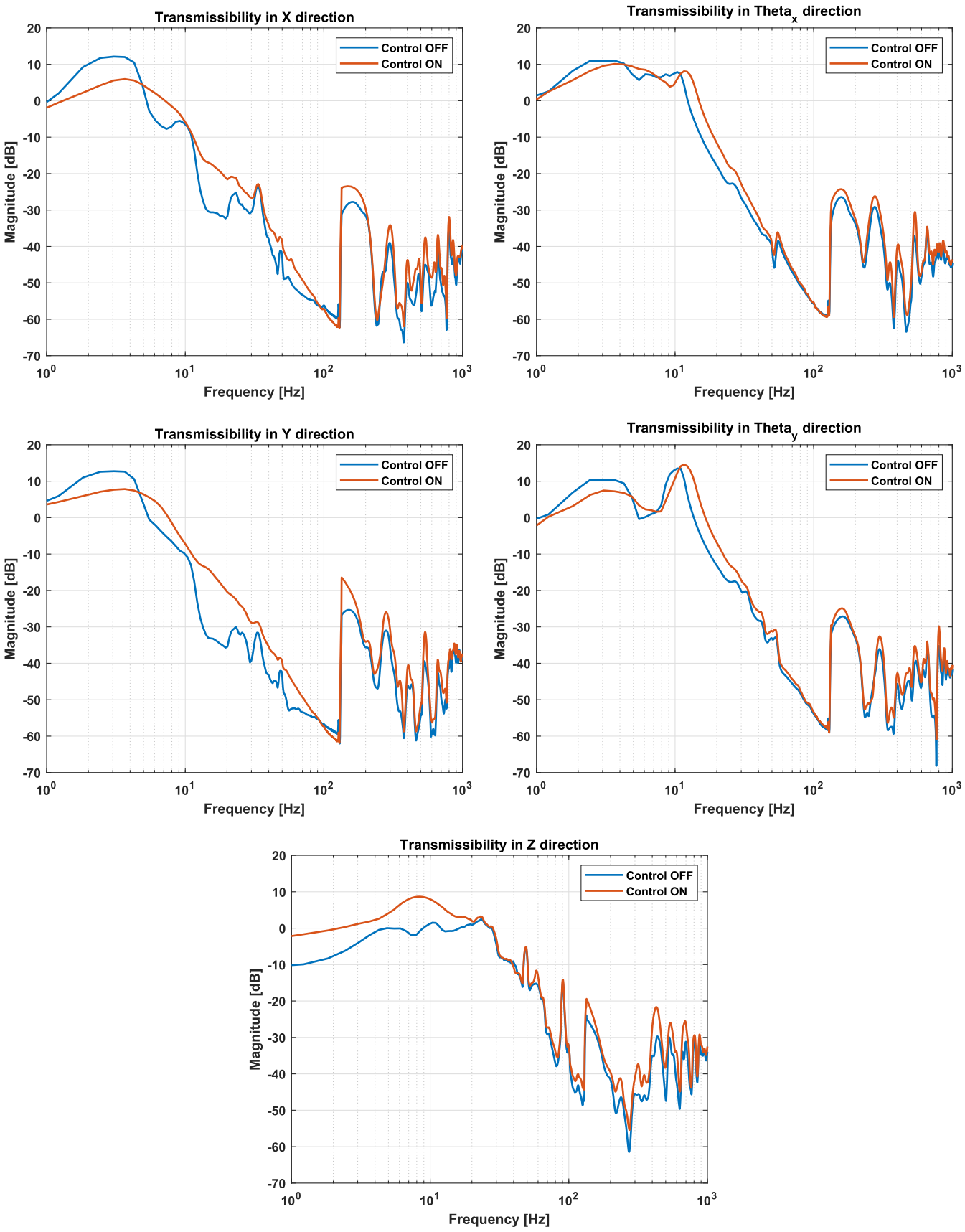

Fig. 22 Transmissibility comparison, control off, and control on for each direction ($X, Y, Z, \theta_x, \theta_y$). Isolation of −60 dB at 130 Hz, limited by background noise >130 Hz.

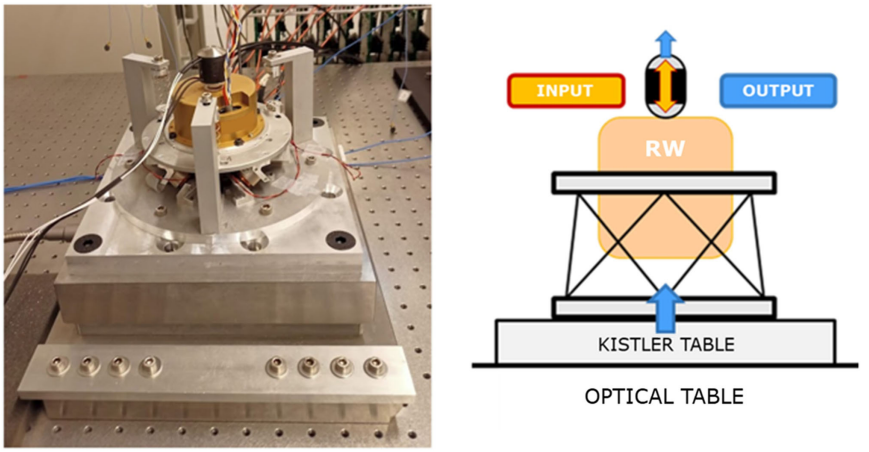

a) b)

Fig. 23 a) Picture of experimental setup with shaker vertically mounted on the reaction wheel; b) corresponding diagram.

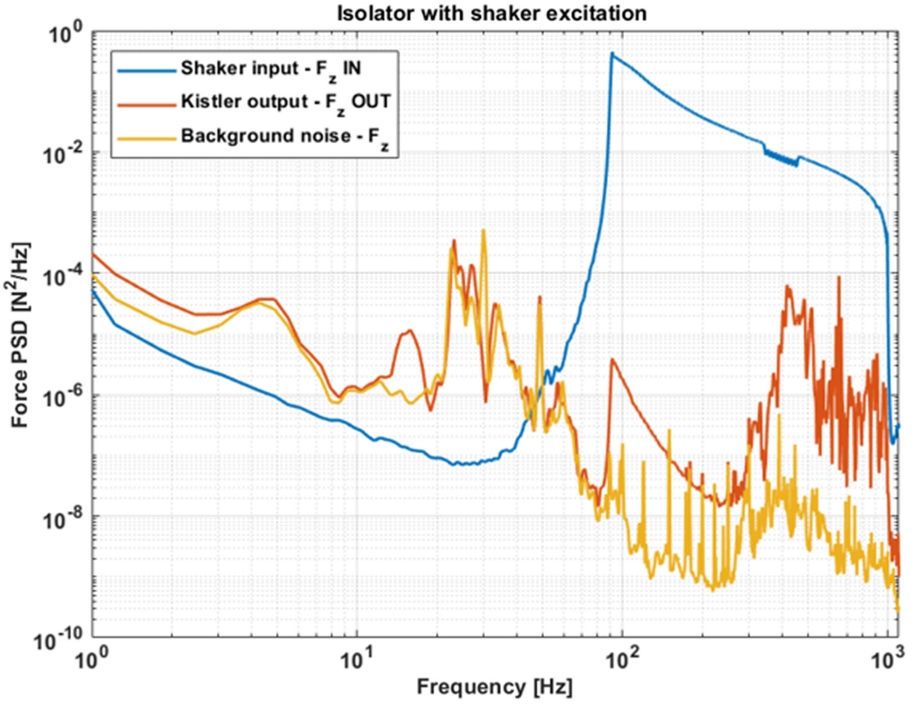

Fig. 24 Forces in the vertical direction measured at the shaker and at the dynamometer. Background noise used to check the effectiveness of the input excitation.

Above 130 Hz, the isolation obtained is degraded, due to the background noise being higher in magnitude than the filtered disturbances coming from the reaction wheel. Another phenomenon affecting the transmissibility is that the peaks of the disturbance with and without the isolation platform are very narrow and occur at slightly shifted frequencies, by which the direct application of Eq. (13) does not correctly give a measure of the real isolation because it does not capture the reduction of the peaks. For these reasons the transmissibilities shown after 130 Hz are computed from the ratio of the envelopes of the Power Spectral Density (PSD). A dashed line has been included in Fig. 21b to indicate the frequency above which enveloping is applied.

Figure 22 shows the reconstructed transmissibilities for the forces in X, Y, and Z and moments around the X and Y axes. The isolator reaches 60 dB of reduction in the transmitted forces and moments at 130 Hz in the X and Y directions, while successfully damping the main resonance of the isolator, most notably reducing the amplifications in the X and Y directions by 7 and 5 dB, respectively. In the Z direction, with active control ON, the performance is degraded when compared to when the active control is OFF. This behavior is caused by the low magnitude of the excitation exerted by the wheel in this

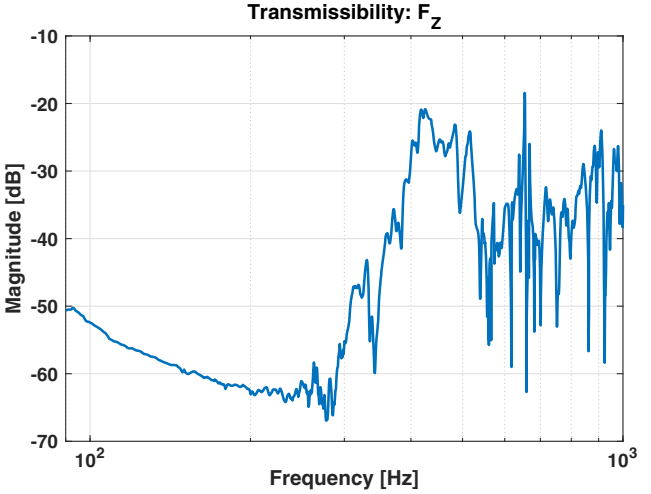

Fig. 25 Zoomed-in (90–1000 Hz) force transmissibility in the vertical direction. Reduction in the transmissibility of 65 dB at 270 Hz, resonance of test setup at 400 Hz.

direction. The active control enables this isolator to take advantage of a low suspension frequency (5 Hz), without exhibiting harmful amplifications at the resonance, creating an early starting point for the steep roll-off of the transmissibility toward higher frequencies. Band-limiting the active control with the NDF controller ensures that damping is only applied at frequencies around the suspension resonance, reducing the overall damping introduced into the system, and therefore mitigating the deterioration of the roll-off due to the added damping. The transmission path for disturbances has been kept free of secondary resonances, ensuring that the magnitude of the transmissibility keeps decreasing as the frequency increases.

To overcome the limited amplitude of disturbance achieved with the functional model of the reaction wheel operating in passive coastdown, supplementary tests were carried out to better characterize the isolation platform. As described next, a minishaker was used to excite the system above the high noise-floor of the test facility occurring at higher frequencies, and the profile of excitation of the reaction wheel model was improved to highlight the benefits of active control in reducing the amplification of the suspension mode down to negligible levels.

C. Supplementary Tests

Extra tests were performed to improve the characterization of the platform shown in Sec. III.B in the axial direction both at low and high frequencies. At high frequency, Fig. 21a shows that the background noise surpasses the magnitude of the excitation injected by the reaction wheel, hampering the characterization of the force transmissibility when using the reaction wheel as an excitation source. It is therefore of interest to use a different excitation source to characterize the performance of the isolator above 130 Hz. At low frequency, the interest is to assess the performance of the active control in the axial direction. The difficulty in exciting the suspension mode of the platform with the passive coastdown of the reaction wheel was overcome by applying a stepped spin-up of the reaction wheel.

To improve the characterization at high frequency in the *Z* direction, the setup shown in Fig. 23 is used. A Siemens Qsources miniature shaker has been glued at the center on top of the reaction wheel housing. This shaker has the advantage of having an embedded force sensor enabling the possibility of directly computing the force

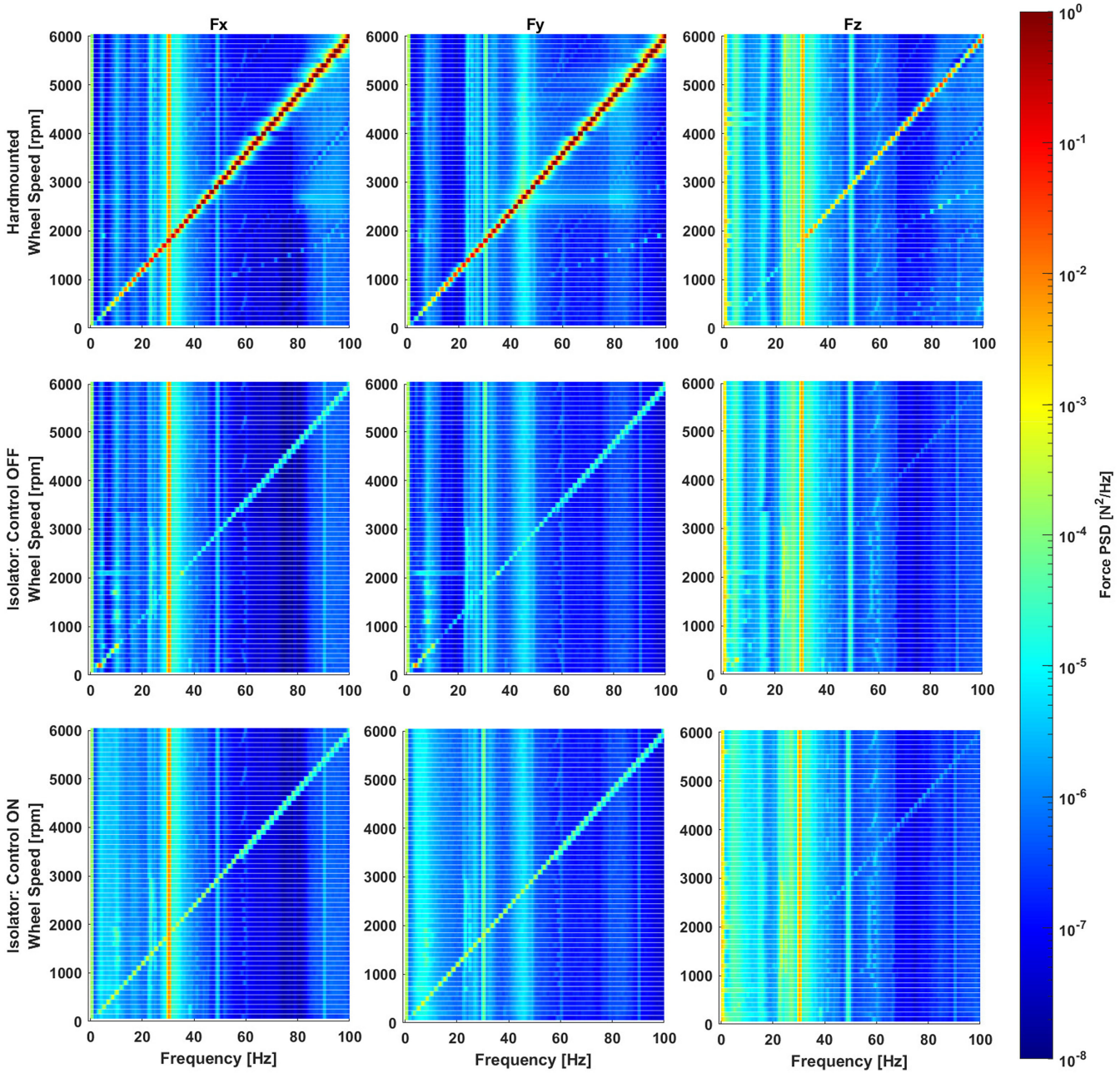

Fig. 26 Contour plots of the force PSD as a function of wheel speed and frequency. Columns = output directions; rows = setup configuration.

transmissibility of the isolator. The test is carried out by injecting white noise into the system, band-passed from 90 to 900 Hz. This frequency band has been chosen to create an overlap with the computed transmissibility below 130 Hz, while ensuring that the frequency band of interest (130–500 Hz) is correctly excited.

As can be observed in Fig. 24, the force measured by the dynamometer is above the background noise threshold in the frequency region where the excitation is applied. The resulting transmissibility between the signals from the shaker's embedded sensor and the dynamometer is shown in Fig. 25. The frequency axis is zoomed on the bandwidth at which the excitation was applied for clarity. A minimum of −65 dB is reached in the transmissibility at 270 Hz, before climbing to −30 dB. The reason for this increase is found in the dynamics of the test setup, which upon testing has been shown to present several resonances in the vertical direction between 400 and 1000 Hz.

The final tests carried out have the objective of investigating the apparent lack of performance of the active control shown in the Z direction while performing the reaction wheel tests (Fig. 22). Due to the nature of a passive coastdown, no constant speed is maintained for an extended period of time, resulting in a lack of consistent excitation at a given frequency, which is exacerbated at low wheel speeds where the reaction wheel coasts to a stop. To tackle this issue, a stepped spin-up of the wheel is carried out. The speed is swept from 100 to 7800 rpm in increments of 100 rpm at intervals of 60 s. While the whole wheel speed range was analyzed for the sake of completeness, the relevant speeds to analyze the low-frequency behavior are from 100 to 600 rpm. These tests have been carried out with the reaction wheel mounted on the isolator, with and without active control. For reference, contour plots corresponding to the stepped spin ups are shown in Fig. 26. A drop in magnitude throughout the whole frequency range can be observed in these plots, with a spike at 5 Hz (observed when the wheel spins at 300 rpm) for the case of the isolated wheel with the active control off due to the undamped suspension resonance of the isolator.

Shown in Fig. 27 are the waterfall plots for the power spectral density of the force in the Z direction as a function of the wheel speed and the frequency. When the isolator is used in passive mode, without active control, a peak of $1.3\text{e}-3\ \text{N}^2/\text{Hz}$ can be seen at the suspension resonance of the system, at 5 Hz when the reaction wheel is spinning at 300 rpm, which is consistent with the excitation from the wheel's unbalance. This peak is reduced to $1.0\text{e}-4\ \text{N}^2/\text{Hz}$ once the active control is turned on, proving that the active control does indeed contribute to the reduction of the amplification at resonance in the Z direction. The reduction in magnitude of the PSD corresponds to a reduction of 5 dB in the transmissibility, which is in line with what has been observed in the X and Y directions during the coastdown tests.

IV. Conclusions

An innovative concept of an active isolation platform for microvibrations was successfully developed and tested. The working principle consisted of the introduction of a suspension mode at low frequencies, i.e., around 5 Hz. The natural roll-off of such a system enabled the isolator to achieve high levels of isolation at high frequency, while the amplification of the suspension modes was artificially damped with active control.

The architecture of this isolation system is based on a Stewart platform. The suspension modes are ensured by the integration of soft springs, while the two sides of the platform isostatically interact in six degrees of freedom via voice-coil actuators. These voice coils are frameless, which guarantees their axial actuation and promotes the mechanical decoupling of the two surfaces of the platform. The actuators are also self-sensing, in which the monitoring of their voltage and current produces an estimate of the relative velocity of the two sides of the platform, thereby enabling the active damping of the suspension modes.

An isolation performance of −65 dB was attained at 270 Hz, when the platform was tested with a shaker in the axial direction. A slight degradation was initially observed when the suspension was tested with the functional model of a reaction wheel, simultaneously disturbing the six degrees of freedom while operating in a passive coastdown (i.e., while measuring the isolation performance when the wheel decelerates passively from its maximum operation speed). These apparent degradations of performance were then dismissed after performing additional tests, where the disturbance levels were increased by exciting with a minishaker and by operating the functional model of the reaction wheel in stepped harmonic excitation.

Future enhancements of this concept can consist of implementation and verification of the functionality of the active alleviation of the launch loads, the scalability required for isolating the microvibrations generated by larger reaction wheels or their assemblies as well as

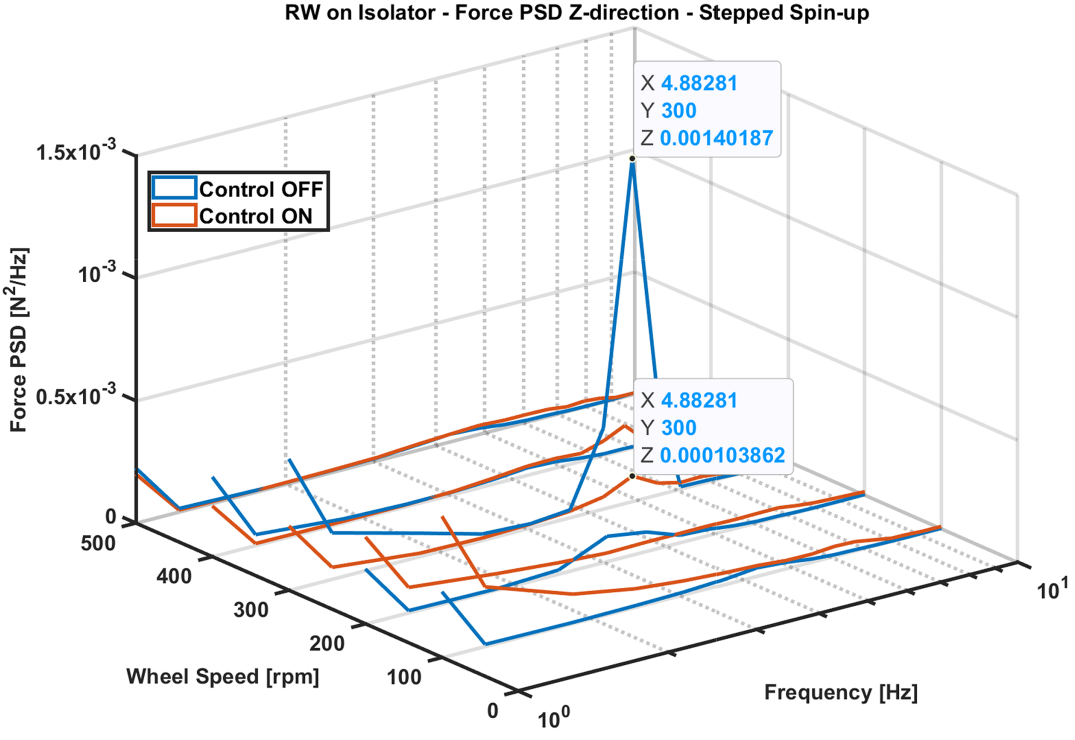

Fig. 27 Waterfall plot of the force in the Z direction during a stepped spin-up. Control off (blue); control on (red).

reducing the natural frequency of the suspension modes, and stiffening of the structural elements in order to improve the overall isolation performance.

Appendix: Equivalence of Force and Motion Transmissibility

The equations of motion of the mass, spring dashpot system with input motion at the base shown in Fig. A1 can be written as

$$ms^2x + cs(x - w) + k(x - w) = F + f \tag{A1}$$

$$F_t = -k(x - w) - cs(x - w) + f \tag{A2}$$

where m is the mass of the system; k is the stiffness; c is the damping; F and f represent an external force acting on the system and the actuator force, respectively; F_t is the transmitted force to the base; x and w are the motion of the mass and the base, respectively; and s is the Laplace variable.

From the above system of equations, the motion transmissibility, force transmissibility, and compliance can be extracted as a function of the actuator force. This is done in order to compare the effect of different control strategies on these transfer functions:

$$\frac{x}{w} = \frac{k + cs}{ms^2 + cs + k} + \frac{1}{ms^2 + cs + k}\frac{f}{w} \tag{A3}$$

$$\frac{F_t}{F} = \frac{-k - cs}{ms^2 + cs + k} + \frac{ms^2}{ms^2 + cs + k}\frac{f}{F} \tag{A4}$$

$$\frac{x}{F} = \frac{1}{ms^2 + cs + k} + \frac{1}{ms^2 + cs + k}\frac{f}{F} \tag{A5}$$

By setting the input force by the actuator to zero, simulating a system without active control, it can be seen that both the motion and force transmissibility are of equal amplitude, with only a difference in sign due to the convention chosen.

To introduce relative motion control into the system, let

$$f = H(s)(x - w) \tag{A6}$$

where $H(s)$ represents the controller used. Substituting Eq. (A6) into Eq. (A3) results in

$$\frac{x}{w} = \frac{k + cs - H(s)}{ms^2 + cs + k - H(s)} \tag{A7}$$

Doing the same with Eq. (A4) requires solving for Eq. (A5) too, resulting in the equations

$$\frac{F_t}{F} = -\frac{k + cs}{ms^2 + cs + k} + \frac{ms^2H(s)}{ms^2 + cs + k}\frac{x}{F} \tag{A8}$$

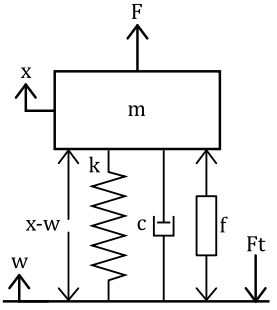

Fig. A1 The 1-DOF system with base motion and input forces as inputs, and mass motion and transmitted force as outputs.

$$\frac{x}{F} = \frac{1}{ms^2 + cs + k - H(s)} \tag{A9}$$

Finally, injecting Eq. (A9) into Eq. (A8) and simplifying results in

$$\frac{F_t}{F} = \frac{H(s) - k - cs}{ms^2 + cs + k - H(s)} \tag{A10}$$

which is analogous to Eq. (A7) although with a factor of -1 due to the sign convention employed.

Acknowledgments

This work has been funded by the European Space Agency through the Networking Partnering Initiative NPI DNI 14894. The authors would like to thank Florian Liebold for his on-boarding and aid at the ESTEC Mechanisms Laboratory, and to the anonymous reviewers for their time, effort, and advice in the development of this paper.

References

[1] Greslou, D., De Lussy, F., Delvit, J., Dechoz, C., and Amberg, V., "Pleiades-HR Innovative Techniques for Geometric Image Quality Commissioning," *International Archives of the Photogrammetry, Remote Sensing and Spatial Information Sciences*, Vol. 39, July 2012, p. B1.

[2] Bronowicki, A. J., "Vibration Isolator for Large Space Telescopes," *Journal of Spacecraft and Rockets*, Vol. 43, No. 1, 2006, pp. 45–53. https://doi.org/10.2514/1.12036.

[3] Arnon, S., and Kopeika, N., "Laser Satellite Communication Network-Vibration Effect and Possible Solutions," *Proceedings of the IEEE*, Vol. 85, No. 10, 1997, pp. 1646–1661. https://doi.org/10.1109/5.640772

[4] Massotti, L., Bulit, A., Daras, I., Dominguez, B. C., Carraz, O., Hall, K., Heliére, A., March, G., Martimort, P., Rodrigues, G., and Silvestrin, P., "Next Generation Gravity Mission Design Activities Within the Mass Change and Geoscience International Constellation," *Sensors, Systems, and Next-Generation Satellites XXVI*, Vol. 12264, SPIE, Bellingham, WA, 2022, pp. 6–17.

[5] Agócs, T., Vanin, F., Laberinti, P., Oetjen, H., Serlenga, D., Sole, M. P., Salenc, C., Lamarre, D., Kaspers, M., Rodrigues, G., and Carou, A. M., "Far-Infrared Outgoing Radiation Understanding and Monitoring (FORUM)–System Overview and Key Technology Developments of ESA's 9 th Earth Explorer," *IGARSS 2022-2022 IEEE International Geoscience and Remote Sensing Symposium*, IEEE, New York, 2022, pp. 7186–7189.

[6] Lux, O., Lemmerz, C., Weiler, F., Kanitz, T., Wernham, D., Rodrigues, G., Hyslop, A., Lecrenier, O., McGoldrick, P., Fabre, F., and Bravetti, P., "ALADIN Laser Frequency Stability and Its Impact on the Aeolus Wind Error," *Atmospheric Measurement Techniques*, Vol. 14, No. 9, 2021, pp. 6305–6333. https://doi.org/10.5194/amt-14-6305-2021

[7] Seiler, R., and Allegranza, C., "Mechanism Noise Signatures: Identification and Modelling," *European Space Mechanisms and Tribology Symposium*, Ruag Aerospace Austria, 2009, Paper 18.

[8] Liebold, F., Wiegand, S., and Käso, R., "Reaction Wheel Disturbance Characterization by Analysis of Micro-Vibration Measurements," *Applied Mechanics and Materials*, Vol. 232, Trans Tech Publ., Germany, 2012, pp. 445–449. https://doi.org/10.4028/www.scientific.net/AMM.232.445

[9] Prashant, A., Madheswaran, M., Kartik, V., Naidu, V. R., Govindan, P., and Aravindakshan, P., "System Development for Micro Vibration Measurements on Spacecrafts," *2016 International Conference on Control, Instrumentation, Communication and Computational Technologies (ICCICCT)*, IEEE, New York, 2016, pp. 98–103.

[10] Masterson, R. A., Miller, D. W., and Grogan, R. L., "Development and Validation of Reaction Wheel Disturbance Models: Empirical Model," *Journal of Sound and Vibration*, Vol. 249, No. 3, 2002, pp. 575–598. https://doi.org/10.1006/jsvi.2001.3868

[11] Le, P. M., "Micro-Disturbances in Reaction Wheels," Ph.D. Thesis, Eindhoven Univ. of Technology, The Netherlands, 2017, https://www.narcis.nl/publication/RecordID/oai:library.tue.nl:856934.

[12] Steier, F., Runte, T., Monsky, A., Klock, T., and Laduree, G., "Managing the Microvibration Impact on Satellite Performances," *Acta Astronautica*,

Vol. 162, Sept. 2019, pp. 461–468.
https://doi.org/10.1016/j.actaastro.2019.06.027
[13] Lin, L., Li, Y., Li, W., Zheng, R., Yanpeng, W., and Xiaoyan, W., "Recent Advances in Precision Measurement & Pointing Control of Spacecraft," *Chinese Journal of Aeronautics*, Vol. 34, No. 10, 2021, pp. 191–209.
https://doi.org/10.1016/j.cja.2020.11.018
[14] Vitelli, M., Specht, B., and Boquet, F., "A Process to Verify the Microvibration and Pointing Stability Requirements for the BepiColombo Mission," *International Workshop on Instrumentation for Planetary Missions*, Vol. 1683, 2012, p. 1023.
[15] Wolf, A., and Dennehy, N., "Applications of Microthrusters on Astrophysics Missions with Demanding Jitter Requirements," *Bulletin of the American Astronomical Society*, Vol. 51, No. 7, 2019, p. 168.
[16] Dennehy, C., and Alvarez-Salazar, O. S., "Spacecraft Micro-Vibration: A Survey of Problems, Experiences, Potential Solutions, and Some Lessons Learned," NASA TM-2018-220075, 2018.
[17] Crede, C., and Ruzicka, J., *Theory of Vibration Isolation Shock and Vibrarion Handbook*, 3rd ed., McGraw-Hill, New York, 1987, Chap. 30.
[18] Sjöberg, M., "On Dynamic Properties of Rubber Isolators," Ph.D. Thesis, Institutionen för farkostteknik, Stockholm, 2002.
[19] Preumont, A., *Vibration Control of Active Structures*, Vol. 2, Springer, Berlin, 1997, pp. 125, 351–356.
[20] Hasha, M. D., "High-Performance Reaction Wheel Optimization for Fine-Pointing Space Platforms: Minimizing Induced Vibration Effects on Jitter Performance Plus Lessons Learned from Hubble Space Telescope for Current and Future Spacecraft Applications," *43rd Aerospace Mechanisms Symposium*, Mechanisms Education Assoc., 2016, Paper 20160008147.
[21] Wilson, J. F., and Davis, L. P., "Viscous Damped Space Structure for Reduced Jitter," *Proceedings 58th Shock and Vibration Symposium*, Department of Defense & NASA, 1987.
[22] Carte, G., "Reaction Wheel Vibration Isolator with Elastomeric Stoppers for Launch Load," *13th European Conference on Spacecraft Structures, Materials & Environmental Testing*, Vol. 727, Braunschweig, 2014, p. 9.
[23] Carte, G., Courgenay, G., Johansson, F., Demerville, T., Mróz, A., Kokot, M., and Rodrigues, G, "Isolation and Damping Systems for Space Application," ESA - DLR, Paper 359424516, 2020.
[24] Kwon, S.-C., Jo, M.-S., and Oh, H.-U., "Experimental Validation of Fly-Wheel Passive Launch and On-Orbit Vibration Isolation System by Using a Superelastic SMA Mesh Washer Isolator," *International Journal of Aerospace Engineering*, Vol. 2017, Jan. 2017, pp. 1–16.
[25] Kamesh, D., Pandiyan, R., and Ghosal, A., "Passive Vibration Isolation of Reaction Wheel Disturbances Using a Low Frequency Flexible Space Platform," *Journal of Sound and Vibration*, Vol. 331, No. 6, 2012, pp. 1310–1330.
https://doi.org/10.1016/j.jsv.2011.10.033
[26] Wei, Z., Li, D., Luo, Q., and Jiang, J., "Performance Analysis of a Flywheel Microvibration Isolation Platform for Spacecraft," *Journal of Spacecraft and Rockets*, Vol. 52, No. 4, 2015, pp. 1263–1268.
https://doi.org/10.2514/1.A33198
[27] Stewart, D., "A Platform with Six Degrees of Freedom," *Proceedings of the Institution of Mechanical Engineers*, Vol. 180, No. 1, 1965, pp. 371–386.
[28] Pendergast, K. J., and Schauwecker, C. J., "Use of a Passive Reaction Wheel Jitter Isolation System to Meet the Advanced X-Ray Astrophysics Facility Imaging Performance Requirements," *Space Telescopes and Instruments V*, Vol. 3356, SPIE, Bellingham, WA, 1998, pp. 1078–1094.
[29] De Marneffe, B., Avraam, M., Deraemaeker, A., Horodinca, M., and Preumont, A., "Vibration Isolation of Precision Payloads: A Six-Axis Electromagnetic Relaxation Isolator," *Journal of Guidance, Control, and Dynamics*, Vol. 32, No. 2, 2009, pp. 395–401.
https://doi.org/10.2514/1.39414
[30] Zheng, Y., Li, Q., Yan, B., Luo, Y., and Zhang, X., "A Stewart Isolator with High-Static-Low-Dynamic Stiffness Struts Based on Negative Stiffness Magnetic Springs," *Journal of Sound and Vibration*, Vol. 422, May 2018, pp. 390–408.
https://doi.org/10.1016/j.jsv.2018.02.046
[31] Spanos, J., Rahman, Z., and Blackwood, G., "A Soft 6-Axis Active Vibration Isolator," *Proceedings of 1995 American Control Conference—ACC'95*, Vol. 1, IEEE, New York, 1995, pp. 412–416.
[32] Davis, L. P., Carter, D. R., and Hyde, T. T., "Second-Generation Hybrid D-Strut," *Smart Structures and Materials 1995: Passive Damping*, Vol. 2445, SPIE, Bellingham, WA, 1995, pp. 161–175.
[33] Hanieh, A. A., "Active Isolation and Damping of Vibrations via Stewart Platform," Ph.D. Thesis, Université Libre de Bruxelles, Active Structures Lab., Brussels, 2003.
[34] Stabile, A., Aglietti, G. S., Richardson, G., and Smet, G., "Design and Verification of a Negative Resistance Electromagnetic Shunt Damper for Spacecraft Micro-Vibration," *Journal of Sound and Vibration*, Vol. 386, Jan. 2017, pp. 38–49.
https://doi.org/10.1016/j.jsv.2016.09.024
[35] Yotov, V. V., Stabile, A., Aglietti, G., Richardson, G., Spanoudakis, P., Cosandier, F., Schwab, P., Wegrzyn, E., De Zanet, G., and Smet, G., "Development and Testing of an Electromagnetic Platform for Microvibration Suppression," *AIAA Scitech 2023 Forum*, AIAA Paper 2023-2067, 2023.
[36] Bronowicki, A., "Forensic Investigation of Reaction Wheel Nutation on Isolator," *49th AIAA/ASME/ASCE/AHS/ASC Structures, Structural Dynamics, and Materials Conference, 16th AIAA/ASME/AHS Adaptive Structures Conference, 10th AIAA Non-Deterministic Approaches Conference, 9th AIAA Gossamer Spacecraft Forum, 4th AIAA Multidisciplinary Design Optimization Specialists Conference*, AIAA Paper 2008-1953, 2008.
[37] Lee, D.-O., Park, G., and Han, J.-H., "Hybrid Isolation of Micro Vibrations Induced by Reaction Wheels," *Journal of Sound and Vibration*, Vol. 363, Feb. 2016, pp. 1–17.
https://doi.org/10.1016/j.jsv.2015.10.023
[38] Geng, Z. J., and Haynes, L. S., "Six DOF Active Vibration Control Using Stewart Platform," *IEEE Transactions on Control Systems Technology*, Vol. 2, No. 1, 1994, pp. 45–53.
https://doi.org/10.1109/87.273110
[39] Spanos, J., Rahman, Z., and Blackwood, G., "A Soft 6-Axis Active Vibration Isolator," *Proceedings of 1995 American Control Conference—ACC'95*, IEEE, New York, 2005, pp. 412–416.
https://doi.org/10.1109/acc.1995.529280
[40] McInroy, J. E., and Hamann, J. C., "Design and Control of Flexure Jointed Hexapods," *IEEE Transactions on Robotics and Automation*, Vol. 16, No. 4, 2000, pp. 372–381.
https://doi.org/10.1109/70.864229
[41] Verma, M., Lafarga, V., and Collette, C., "Perfect Collocation Using Self-Sensing Electromagnetic Actuator: Application to Vibration Control of Flexible Structures," *Sensors and Actuators A: Physical*, Vol. 313, Oct. 2020, Paper 112210.
https://doi.org/10.1016/j.sna.2020.112210
[42] Cazzulani, G., Resta, F., Ripamonti, F., and Zanzi, R., "Negative Derivative Feedback for Vibration Control of Flexible Structures," *Smart Materials and Structures*, Vol. 21, No. 7, 2012, Paper 075024.
https://doi.org/10.1088/0964-1726/21/7/075024
[43] Jamshidi, R., and Collette, C., "Optimal Negative Derivative Feedback Controller Design for Collocated Systems Based on H2 and H_∞ Method," *Mechanical Systems and Signal Processing*, Vol. 181, Dec. 2022, Paper 109497.
https://doi.org/10.1016/j.ymssp.2022.109497
[44] Stoica, P., and Moses, R. L., *Spectral Analysis of Signals*, Pearson Prentice Hall, Upper Saddle River, NJ, 2005, p. 87.

M. A. Ayoubi
Associate Editor